INNER-SHELL PHOTOEMISSION FROM ATOMS AND MOLECULES
USING SYNCHROTRON RADIATION

Dennis William Lindle
(Ph.D. Thesis)

Materials and Molecular Research Division
Lawrence Berkeley Laboratory
and
Department of Chemistry
University of California
Berkeley, California 94720

DISCLAIMER

INNER-SHELL PHOTOEMISSION FROM ATOMS AND MOLECULES
USING SYNCHROTRON RADIATION

Dennis William Lindle

Materials and Molecular Research Division
Lawrence Berkeley Laboratory
and
Department of Chemistry
University of California
Berkeley, California 94720

Abstract

Photoelectron spectroscopy, in conjunction with synchrotron
radiation, has been used to study inner-shell photoemission from atoms
and molecules. The time structure of the synchrotron radiation
permits the measurement of time-of-flight (TOF) spectra of Auger and
photoelectrons, thereby increasing the electron collection efficiency.
The double-angle TOF method yielded angle-resolved photoelectron
intensities, which were used to determine photoionization cross
sections and photoelectron angular distributions in several cases.
Comparison to theoretical calculations has been made where possible to
help explain observed phenomena in terms of the electronic structure
and photoionization dynamics of the systems studied.

Measurements have been made for the 3d subshell in krypton, the
iodine 4d and 4p subshells in methyl iodide, the nitrogen K shell in
N_2 and NO, and the main and satellite lines in helium. For the Kr
3d subshell, angular-distribution asymmetry parameters are presented
for photon energies from 100 to 600 eV which show large changes

attributable to important one-electron effects. The asymmetry parameter fell below the Hartree-Fock-theory prediction at high photon energy, and showed resonant interchannel-coupling effects near the 3p threshold. The total intensity of shake-up satellites relative to the Kr 3d main line decreased with photon energy in the range 180 to 270 eV, and the average asymmetry parameter for these satellite states showed a marked increase over the same energy range.

For methyl iodide, the first photoemission measurements on the I 4d and I 4p subshells are presented. Cross sections and asymmetry parameters were measured from threshold to 300 eV photon energy for the I 4d level (to 440 eV for the asymmetry parameter), and from 175 to 300 eV for the I 4p level. The I 4d results exhibited atomic-like behavior throughout this energy range, mimicking similar behavior for the Xe 4d subshell and indicating that the I 4d subshell is localized on the iodine atom in CH_3I. Near threshold, the spin-orbit final states, $4d_{5/2}$ and $4d_{3/2}$, were resolved and exhibited non-statistical intensity ratios mainly due to a kinetic-energy effect. The I 4p asymmetry-parameter results were essentially identical to the asymmetry-parameter results for the I 4d subshell at the same photon energy, suggesting strong interchannel coupling, despite the fact that the I 4p cross section is of the same order as the I 4d cross section in the energy range measured.

Also reported are the first gas-phase photoemission measurements near the nitrogen K edges of N_2 and NO. Shape-resonance behavior was observed in the cross sections for both N 1s photoemission and N

KVV Auger emission. The asymmetry parameters for N 1s photoemission show larger contrast ratios than the cross-section data, and agree with multiple-scattering calculations except for a small energy shift.

In He, the partial cross section, the satellite branching ratio, and the asymmetry parameter for simultaneous photoionization and excitation to the n=2 states of the He^+ ion have been measured in the energy range directly above threshold. The asymmetry-parameter results have been used to determine the ratio of the cross sections for producing the 2p final state versus the 2s final state; the He^+(n=2) satellite was shown to be predominantly 2p near threshold, in agreement with the experimental and most of the theoretical results reported to date. In the region below the He^+(n=3) threshold at 73 eV, the effects of a series of autoionizing Rydberg levels on the cross sections and asymmetry parameters for the n=2 satellites were observed, this being the first detailed measurement of the angular distribution of a satellite over an autoionization resonance. Parameters defining all of the measured resonance profiles were obtained, and in particular, some individual dipole matrix elements were derived from the experimental results.

David A. Shirley

Table of Contents

I. INTRODUCTION

Photoelectron spectroscopy, in which electrons ionized by photon impact are studied, is an excellent tool for determining the electronic properties (structure and dynamics) of atoms and molecules. The directness of this technique for studying electronic structure is illustrated by the very simple idea, first proposed by Koopmans,[1] that the ionization potential, I_j, of an electron in a bound orbital, j, is equal in magnitude to the one-electron orbital energy, E_j,

$$I_j = -E_j . \tag{1}$$

This good first approximation provides that the measurement of I_j's can yield a direct representation of the orbital energy diagram of an atom or molecule. Koopmans' theorem is especially helpful for studies that attempt to determine electronic structure only.[2,3] The understanding of the dynamics of the photoionization process, however, necessitates going beyond Koopmans' theorem and electronic-structure measurements, and generally requires more sophisticated experimental and theoretical techniques. The majority of the work along these lines has been concerned with electrons in valence orbitals.[4] This dissertation presents results of experimental studies of photo-ionization dynamics in an area in which relatively little work has been done; inner-shell photoemission from atoms (Kr and He) and molecules (CH_3I, N_2, and NO).

A photoelectron spectrum is a plot of the number of electrons

emitted by photoionization as a function of their kinetic energy,
ϵ_j. For a given photon energy, $h\nu$, the photoelectron spectrum is
characterized by a discrete set of photoemission peaks as a
consequence of the energy-conservation expression

$$\epsilon_j = h\nu - I_j . \tag{2}$$

Recourse to Eq. (1) and an appropriate theoretical energy-level
calculation then may yield an association of each peak in the spectrum
with a particular final state of the resulting ion. This constitutes
a determination of electronic structure. More information may be
gained by taking photoelectron spectra at many different photon
energies. For example, peak intensities as a function of photon
energy are proportional to the photoionization cross section.
Neglecting all but electric-dipole interactions,[5] the cross section,
$\sigma_j(\epsilon)$, for ionizing an electron from orbital j (or equivalently, for
producing the ionic state j, where the ion has lost an electron from
orbital j) is given by[6]

$$\sigma_j(\epsilon) = \frac{4\pi^2 \alpha a_0^2}{3} (\epsilon_j + I_j) \sum_k |\langle \psi_j^{(N-1)} \phi_k(\epsilon) | \sum_{\mu=1}^{N} \vec{r}_\mu | \psi_i^{(N)} \rangle|^2 , \tag{3}$$

where α is the fine-structure constant, a_0 is the Bohr radius,
$\psi_j^{(N-1)}$ is the (N-1)-electron wavefunction of the ion, the ϕ_k
are single-electron wavefunctions of the possible continuum states k
of the photoelectron, $\vec{r}_\mu$ is the dipole operator, where μ represents

the coordinates of each electron in the ground state, i, and $\psi_i^{(N)}$
is the N-electron ground-state wavefunction of the neutral atom or
molecule. Equation (3) shows that the cross section is an incoherent
sum of dipole matrix elements between the initial ground state and the
final ion-continuum electron states. Dependence of the cross section
on the photon energy is included both explicitly, in the term
$r_j + I_j$ (= $h\nu$), and implicitly in the energy-dependent functions
$\phi_k(\epsilon)$ within the matrix elements. It is this feature, the photon-
energy dependence of the cross section (and other parameters), that
reveals the dynamics of the photoionization process.

Aside from the photoionization cross section, each photoelectron
peak can be characterized by its spatial or angular distribution. For
randomly oriented gas-phase atoms or molecules ionized by linearly
polarized radiation, Yang's theorem yields[7]

$$\frac{d\sigma_j(\epsilon)}{d\Omega} = \frac{\sigma_j(\epsilon)}{4\pi} [1 + \beta_j(\epsilon)P_2(\cos \theta)] , \tag{4}$$

where $d\sigma_j(\epsilon)/d\Omega$ is the differential cross section in the solid angle
Ω, θ is the angle between the photoelectron propagation vector and the
polarization vector of the ionizing radiation, $P_2(\cos \theta)$ is the
second Legendre polynomial $[1/2(3\cos^2\theta - 1)]$, and $\beta_j(\epsilon)$ is the
angular-distribution asymmetry parameter. Within the dipole approx-
imation, the asymmetry parameter completely describes the angular
distribution of photoelectrons. The requirement that the differential
cross section remain non-negative restricts $\beta_j(\epsilon)$ to the range -1 to

2. Because $\beta_j(\epsilon)$ is not an angle-integrated quantity, it may depend on the coherent sum of dipole matrix elements, in contrast to $\sigma_j(\epsilon)$. Thus, the measurement of asymmetry parameters yields complementary information to cross-section data, and generally the asymmetry-parameter results show more dramatic energy-dependent changes as a consequence of the phase interference introduced by the coherent summing of matrix elements.

The goal of this work has been the study of photon-energy dependent behavior of cross sections and asymmetry parameters for inner shells of atoms and molecules in order learn more about single-electron, resonant, and multi-electron effects in photoionization. The remainder of this chapter will discuss briefly the different types of effects that influence the results presented in Chapters III-VI. For convenience, a distinction is made between single-electron and multi-electron processes. The former are of interest to an analysis of photoionization dynamics; the latter to the understanding of electron-correlation phenomena.

The single-electron approximation assumes that the initial ground state of an atom or molecule can be described adequately by a product of one-electron orbital wavefunctions, and that photoionization corresponds to removal of an electron from one of these orbitals. From Eq. (3), this implies that the cross section is dependent on a set of one-electron matrix elements, which can be approximated as modified overlap matrix elements between the initial and continuum wavefunctions. This latter assumption provides a particularly simple

picture within which to understand the energy dependence of cross
sections and asymmetry parameters. For example, photoionization of Kr
3d electrons to ϵf photoelectrons,[8] where ϵ denotes that this is a
continuum f channel, experiences a strong change with energy from
threshold to ~30 eV above threshold (see Chapter III). This behavior
can be related to the changing overlap of the initial state with the
continuum $\ell=3$ wavefunction; the overlap is poor at low kinetic
energies because of the centrifugal repulsion of the $\ell=3$ wavefunction
by the atomic nucleus, but increases at higher energies. This
interaction of the photoelectron with the atomic potential causes the
Kr 3d asymmetry parameter to vary rapidly in this energy range.

Similar, but more dramatic, effects can be observed when the
potential experienced by the photoelectron contains a barrier as a
result of the interplay of the Coulomb attraction and the centrifugal
repulsion between the nucleus and the photoelectron. The barrier
enhances the overlap of the initial and continuum states at certain
energies, leading to very strong oscillations in both the cross
section and asymmetry parameter. These changes are referred to as
shape-resonance phenomena, because of their dependence on the shape of
the potential. Measurements on the atomic-like I 4d subshell in
CH_3I[9] (Chapter IV) indicate that the cross section is low near
threshold, where the photoelectron can be thought of as being trapped
by the potential barrier, and increases ten-fold at higher energies.
The I 4d asymmetry parameter also shows large changes in this energy
range.

Shape resonances also influence molecular photoionization, with the important difference that the molecular potential is intrinsically anisotropic. Therefore, molecular shape-resonance behavior, particularly changes in the asymmetry parameter, may provide a fingerprint of the molecular potential. Another important difference between atomic and molecular shape resonances is that the vibrational modes available to molecules tend to weaken the effects of shape resonances on cross sections and asymmetry parameters. Chapter V presents the first photoemission measurements of any gas-phase species near the N 1s threshold. The results for N_2 and NO are interpreted in terms of shape-resonance phenomena.

Another category of single-electron effects can be understood by reference to Eq. (3). If a term in the summation changes sign by virtue of a change in wavefunction overlap with energy, that term will be zero at some energy, as initially elucidated by Cooper.[10] The result is a local minimum in the cross section at the energy of the zero crossing. If the term affected is the dominant one, a pronounced Cooper minimum in the cross section is observed and large changes in the asymmetry parameter will occur. This interpretation is used to describe the cross-section and asymmetry-parameter results for the I 4d subshell of CH_3I (Chapter IV) for photon energies above ~150 eV.

Photoionization processes that involve more than one electron generally occur with less intensity than those involving only a single electron, making experimental measurements more difficult. Nevertheless, where feasible, these experiments yield a wealth of

information on electron-electron correlation and intershell inter-
actions. An example of the latter can be found in Chapter IV, where
photoionization of the I 4p subshell in CH_3I is discussed. The
behavior of the I 4p asymmetry parameter is remarkable because it
closely mimics the I 4d asymmetry parameter, suggesting that an
intimate coupling between the 4d and 4p subshells is present. Partial
understanding of this phenomenon is possible with the realization that
the I 4p peak is not produced by a single-electron process, but can be
identified to some extent with a multi-electron process yielding a
$4d^8 4f$ final state. This measurement documents one of the most
pronounced interchannel interactions observed to date.

Electron correlation leads to a breakdown of the Koopmans picture
of photoelectron spectra; peaks appear that correspond to the
ionization of one electron accompanied by the excitation of a second
electron to a higher-lying orbital. These 'satellite' peaks are
usually less intense ($\leq 20\%$) than the main single-electron peaks, and
their intensities are derived solely from multi-electron interactions.
Although much work has been done to determine the energies and
configurations of satellite peaks, very little is known (experimentally
or theoretically) about the energy dependences of their cross sections
and angular distributions. In the high-energy or sudden limit, the
shake-up model[11] has been used with some success in predicting
satellite intensities. At lower energies, for which the photoelectron
may interact significantly with the remaining electrons, processes
other than shake-up may be important, and the exact identification of

the contributions to satellite formation is beyond the present understanding. The results for satellites in He (Chapter VI) and Kr (Chapter III) constitute a considerable fraction of the existing energy-dependent satellite measurements. In both cases, changes in the cross sections and asymmetry parameters with photon energy have been observed. For He, these changes are explained in terms of an additional low-energy mechanism for satellite production (other than shake-up) that is most important near threshold.

The photoionization studies of the He satellites also include measurements of the resonance behavior of cross sections and asymmetry parameters. The resonances are Rydberg-like states [eg. He*(3s3p)] in which both electrons are excited. The He* atom then decays to the He$^+$ ion by the autoionization process; one electron escapes, the other electron relaxes to a 2s or 2p orbital, leaving the He$^+$(n=2) satellite states. In general, autoionization is an interference phenomenon because of the two pathways, direct ionization and ionization through the intermediate resonant state, by which the system can pass from the initial to the final state. The interference causes asymmetric profiles in both the cross section and asymmetry parameter as a function of energy (see Chapter VI) that are quantitatively indicative of the matrix elements governing the autoionization process, and in favorable cases such as He, some of these matrix elements can be extracted from the experimental results.

The next chapter presents some experimental details that are common to the results discussed in Chapters III-VI.

REFERENCES

1. T. Koopmans, Physica 1, 104 (1933).

2. D.W. Turner, A.D. Baker, C. Baker, and C.R. Brundle, Molecular Photoelectron Spectroscopy (Wiley, New York, 1970).

3. K. Siegbahn, C. Nordling, G. Johansson, J. Hedman, P.F. Hedén, K. Hamrin, U. Gelius, T. Bergmark, L.O. Werme, R. Manne, and Y. Baer, ESCA Applied to Free Molecules (North-Holland, Amsterdam, 1969).

4. J. Berkowitz, Photoabsorption, Photoionization, and Photoelectron Spectroscopy (Academic Press, New York, 1979).

5. This is the dipole approximation (also referred to as neglect of retardation). It is a good assumption for photon energies used in this work (≤ 600 eV). See Ref. 6.

6. S.T. Manson, in Advances in Electronics and Electron Physics 41, 73 (1976).

7. C.N. Yang, Phys. Rev. 74, 764 (1948).

8. The selection rules for atomic photoionization require that an $n\ell$ bound electron be ionized to an $\epsilon(\ell\pm1)$ continuum state. The $\ell+1$ channel is usually dominant.

9. The effect of the methyl group on I 4d ionization is small, and the results in Chapter IV are explained adequately in terms of an atomic-like shape resonance.

10. J.W. Cooper, Phys. Rev. 128, 681 (1962).

11. Shake-up refers to the photoionization model in which the photoelectron has high kinetic energy and leaves the ionic core

quickly. The remaining electrons are 'shaken' by the sudden
change in potential, in some cases being excited to form satellite
states.

II. EXPERIMENTAL

Gas-phase photoelectron spectroscopy requires the coupling of a photon source, an apparatus to deliver the gaseous sample for interaction with the radiation, and an electron energy analyzer. For the experiments described in this dissertation, monochromatized synchrotron radiation was used as the photon source, gases were delivered by an effusive gas jet, and the electrons were detected by time-of-flight (TOF) analysis. All of the components and methods used for these experiments have been described previously,[1-7] therefore this chapter will review only the major aspects of the technique.

All of the measurements were made at the Stanford Synchrotron Radiation Laboratory (SSRL) during discrete 'runs' approximately two weeks long a few times a year. This type of schedule was conducive to long hours, little sleep, and hectic experiments. Nonetheless, during my tenure, 11 runs were performed with the TOF apparatus (see Table 1, Chapter II of Ref. 5), which included over 30 successful experiments. Figure 1 is a photograph of the individuals who were responsible for most of these successes.

The characteristics of synchrotron radiation have been described by Winick.[8] Briefly, the radiation produced by SPEAR is a moderately intense continuum source from visible to hard X-ray wavelengths. Additional advantages are provided by the inherent polarization of synchrotron radiation and the excellent time structure (0.3 nsec pulses every 780 nsec in single-bunch running) available at SPEAR.

Some disadvantages of working with synchrotron radiation pertinent to
gas-phase photoelectron spectroscopy are discussed by Southworth.[3]
I share with him 'the wonder of it all' when everything worked at the
same time. Somehow it seemed to make working at SSRL worth it.

After leaving the storage ring, the synchrotron radiation is
deflected to a monochromator for energy dispersion and selection. All
of the experiments in this dissertation were performed with the
grazing-incidence Rowland-circle 'grasshopper' monochromator on Beam
Line III-1[9] at SSRL. It was operated with a 1200 line/mm
holographically-ruled grating, yielding a useful energy range of 50 to
maybe as high as 600 eV (at the higher energies, the photon resolution
is _very_ poor). The monochromator is equipped with adjustable entrance
and exit slits that allow the experimenter to select the desired
photon resolution, while of course, giving up significant amounts of
photon flux.

The monochromatized photon beam then enters the TOF chamber and
intersects an effusive gas jet of the sample to be studied. The
electrons emitted in the interaction region are detected by identical
TOF analyzers at two angles, $0°$ and $54.7°$, with respect to the
polarization vector of the radiation. The overall scheme is depicted
in Fig. 2. The gas jet normally was positioned vertically with the
nozzle below the photon beam. Typical pressures in the interaction
region were estimated to be $1-5 \times 10^{-3}$ torr, approximately an order
of magnitude larger than the ambient chamber pressure. The pressure
behind the jet's nozzle was monitored by a capacitance manometer (to

better than ±5%) that also automatically controlled the flow rate of
the gas into the chamber. To protect the ultrahigh-vacuum monochro-
mator and storage ring from the ~10^{-4} torr in the experimental
chamber, it was necessary to interpose an ultrathin Al window (1500Å
thick) to separate the two vacuum regions. To protect this window, an
elaborate interlock system (pressure sensors, fast-closing valves,
etc.) was developed. We pride ourselves in never having broken one
during regular operation, although at other (less dangerous) times,
the delicate windows seemed particularly susceptible to clumsiness.
The separation of our vacuum system from that of SSRL permitted
moderately worry-free running, but with the disadvantage of some
photon absorption. The transmission of the Al window is shown in Fig.
3. The structure at 72 eV is due to the $L_{2,3}$ edge of Al metal.
This scan was taken by monitoring the photon flux at the back of the
TOF chamber with a sodium salicylate scintillator and an optical
photomultiplier tube (RCA 8850). The response of the sodium
salicylate is constant up to 120 eV,[10] above which no measurements
are available. Initial indications are that the response increases at
higher photon energies, which would require corrections to be made to
some of our cross-section measurements.

Electrons emitted in the interaction region were energy analyzed
by virtue of the different flight times, t, for electrons with
different kinetic energies, ε, according to

$$t = \frac{CL_t}{\varepsilon^{1/2}} \, , \tag{1}$$

where L_t is the length of the flight path of the TOF analyzers (~29 cm), and C is a constant. This method works at SSRL because the synchrotron radiation is pulsed as a result of the bunched structure of the electrons in the storage ring. The pulses are narrow (~0.3 nsec) and spaced far enough apart in time (195-780 nsec depending on the running mode of SPEAR) to allow electrons of most energies to be collected between consecutive pulses with moderate-to-good time resolution. The limitation on the TOF analyzer resolution at low electron kinetic energies is the uncertainty in the flight path (and hence the flight time) because of the finite width (3 mm) of the photon beam at the interaction region. For the grasshopper mono-chromator, the resolution was typically 2.5% of the kinetic energy of the electrons for the 0° analyzer, and 3.5-4.0% for the 54.7° detector. At high kinetic energies (>100-200 eV), other contributions to the resolution become important, and the poor overall analyzer resolution is prohibitive to doing well-resolved experiments.

The TOF method is well-suited to gas-phase photoelectron spectroscopy because it collects nearly all energies of photoelectrons simultaneously, providing an excellent signal-to-noise ratio for many experiments. Simultaneous measurement of photoelectron peak intensities at two angles yields asymmetry parameters (see Eq. 4, Chapter I) that are independent of variations in the photon flux and gas pressure. Peak intensities at 54.7° (the 'magic angle'), for which $P_2(\cos \theta)$ vanishes, are directly proportional to photoion-ization cross sections after normalization to photon flux and gas

pressure. Comparison of intensities of two peaks in the same 54.7°
spectrum (branching ratios) alleviates the problem of normalization.
In order to place the asymmetry-parameter measurements on the correct
scale, it is necessary to calibrate the apparatus by measuring known
values of β. For this purpose, we used the asymmetry parameters for
Ne 2p and 2s ionization,[11] deriving from them a curve describing the
relative efficiency of the two analyzers operating in the double-angle
TOF mode. This procedure has been described in detail previously.[3-7]
It is important to note that this greatly reduces the effects of
systematic errors on the measurements of unknown asymmetry parameters.
For example, the effect of some nonlinear polarization on the β
measurements is virtually negligible as long as the degree of linear
polarization is greater than ~75%. The actual polarization of the
grasshopper monochromator has been estimated to be 98%.[3,7] Total
systematic errors for β for all of the measurements in this disser-
tation are estimated to be ±0.10 or less. A similar correction must
be applied to the cross-section and branching-ratio measurements
because of the energy-dependent transmission of the 54.7° analyzer.
The transmission is determined simultaneously with the efficiency
function by using the known values of the cross section for Ne L-shell
ionization.[11] Systematic errors for the cross-section and branching-
ratio results are estimated to be 10-15% of the reported value for
each data point.

The remaining chapters deal with individual experiments that were
performed during the Fall of 1981 and the Spring of 1982; Kr (Chapter

III), CH_3I (Chapter IV), N_2 and NO (Chapter V), and He (Chapter VI). Additional experimental details pertinent to a given experiment may be found in these chapters.

REFERENCES

1. M.G. White, Ph.D. Thesis, University of California, Berkeley (1979); Lawrence Berkeley Laboratory report No. LBL-9527.

2. M.G. White, R.A. Rosenberg, G. Gabor, E.D. Poliakoff, G. Thornton, S.H. Southworth, and D.A. Shirley, Rev. Sci. Instrum. 50, 1268 (1979).

3. S.H. Southworth, Ph.D. Thesis, University of California, Berkeley (1982); Lawrence Berkeley Laboratory report No. LBL-13512.

4. S. Southworth, C.M. Truesdale, P.H. Kobrin, D.W. Lindle, W.D. Brewer, and D.A. Shirley, J. Chem. Phys. 76, 143 (1982).

5. P.H. Kobrin, Ph.D. Thesis, University of California, Berkeley (1983); Lawrence Berkeley Laboratory report No. LBL-15591.

6. C.M. Truesdale, Ph.D. Thesis, University of California, Berkeley (1983); Lawrence Berkeley Laboratory report No. LBL-15902.

7. S.H. Southworth, U. Becker, C.M. Truesdale, P.H. Kobrin, D.W. Lindle, S. Owaki, and D.A. Shirley, Phys. Rev. A 28, 261 (1983).

8. H. Winick, in Synchrotron Radiation Research, ed. by H. Winick and S. Doniach (Plenum, New York, 1980).

9. F.C. Brown, R.Z. Bachrach, and N. Lien, Nucl. Instrum. Meth. 152, 73 (1978).

10. J.A.R. Samson and G.N. Haddad, J. Opt. Soc. Am. 64, 1346 (1974).

11. F. Wuilleumier and M.O. Krause, J. Electron Spectrosc. 15, 15 (1979).

FIGURE CAPTIONS

Fig. 1. Picture taken during the Spring of 1981 at SSRL. From left:
Carlton "Trues" Truesdale, Dennis Lindle, Uwe Becker, Steve
Southworth, and Paul Kobrin.

Fig. 2. Schematic of the double-angle time-of-flight (DATOF) method.

Fig. 3. The relative photon flux from the grasshopper monochromator
after passing through the Al window (solid curve). The dashed
curve is the relative flux through a vitreous-carbon window
that has been used only since the present experiments were
completed. Both scans were taken as described in the text.
The dip in flux at ~280 eV for the Al window is due to the
K-edge absorption of carbon adsorbed on the surfaces of the
optical elements in the beam line.

CBB 815-4462

Figure 1
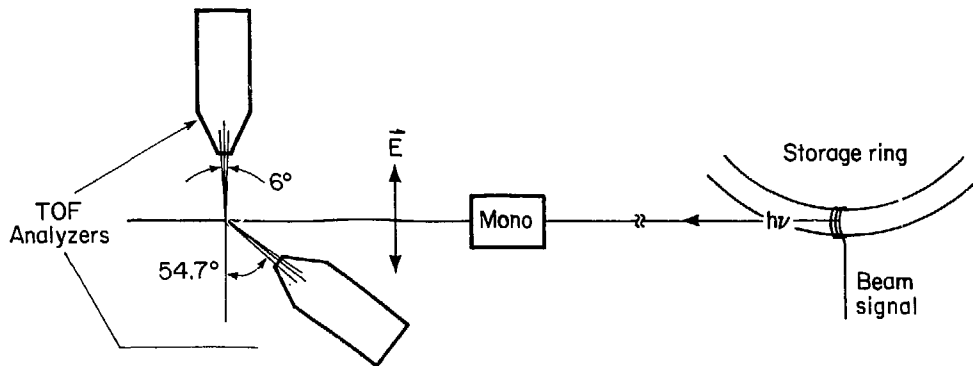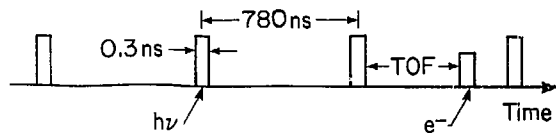
XBL 7910-4225

Figure 2
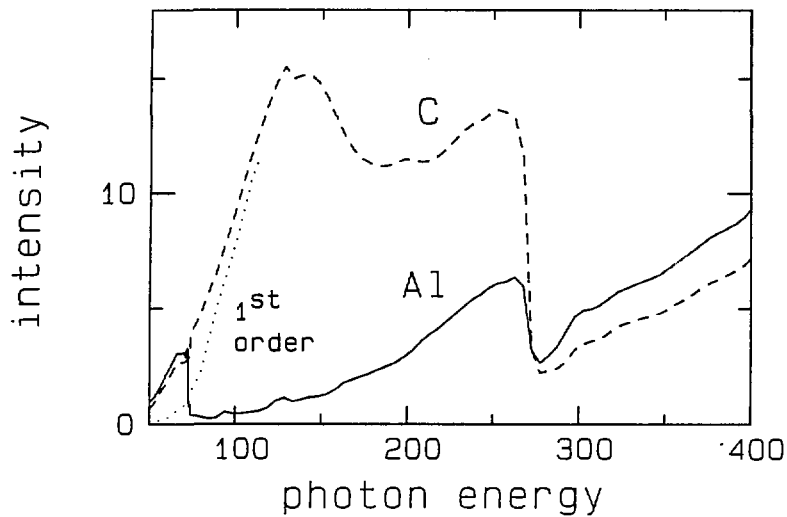
Figure 3

III. PHOTOEMISSION FROM THE 3d SUBSHELL OF ATOMIC Kr*

Recent photoemission measurements on the inner shells of Xe,[1,2] Hg,[3] and I in CH_3I[4] have exhibited oscillations in the energy-dependences of angular distributions that are caused by interaction of the photoelectron with the atomic potential. In particular, a centrifugal barrier produces a strong shape-resonance effect in the asymmetry parameters for the 4d and 4f states in the above systems. Although no centrifugal barrier is present for atomic Kr because of the smaller Coulomb attraction in this lower-Z element, similar effects are expected based on the shape of the repulsive part of the potential.[5] We report here measurements confirming this expectation for the Kr 3d asymmetry parameter. Also included are results indicating the importance of multi-electron effects; interchannel coupling of the 3d and 3p subshells, and production of satellites of the 3d main line. For the latter, relative intensities and asymmetry parameters are presented which show significant changes as a function of energy.

A TOF spectrum of Kr taken at 224 eV photon energy is shown in Fig. 1. This spectrum is dominated by features associated with 3d subshell photoionization; the unresolved 3d photoemission lines with binding energies of 93.7 eV ($4d_{5/2}$) and 94.9 eV ($4d_{3/2}$),[6] a satellite peak of the 3d line, mostly composed of $4p \rightarrow 5p$ shake-up states (~114 eV binding energy[7]), and all of the Auger features below 60 eV kinetic energy. Evidence of 3p ionization (thresholds at

214.4 and 222.2 eV[6]) is apparent with the $M_{2,3}M_{4,5}N$ Auger peak. The remaining high-energy peaks result from photoionization of the valence subshells and from photoemission induced by higher-order components of the synchrotron radiation.

Figure 2 displays the measured asymmetry parameters for 3d photoionization along with previous measurements by Krause[8] and Carlson et al.[9] At certain photon-energy settings of the monochromator, a component of second-order radiation (energy of 2hν) was large enough to produce peaks in our spectra, primarily second-order peaks of Kr 3d photoionization. Because the β measurements are independent of the photon flux, we were able to extend our β_{3d} results to higher photon energies. At low energies, we observe excellent agreement with the earlier data,[9] whereas the earlier higher-energy results[8] are systematically larger than the present data. Comparison with Hartree-Fock velocity (HF-V)[10] and relativistic random-phase approximation (RRPA)[11] calculations also is made in Fig. 2. The theoretical curves nearly coincide from threshold to 125 eV, both showing good agreement with the experimental results. Above 200 eV, the HF-V calculation overestimates the asymmetry parameter measured here, but agrees rather well with the earlier measurements.[8] The minimum in β_{3d} at 115-120 eV can be ascribed to a potential-barrier effect on the εf photoelectron channel.[5,12] Near threshold, the centrifugal barrier for an ℓ=3 continuum wavefunction inhibits the εf channel. As the energy increases, this channel rapidly begins to dominate the photoionization process, including a subsequent change in the

asymmetry parameter.[13] The concurrence of the theoretical results with the experimental measurements at low energy confirms this interpretation, as well as indicating that Kr 3d photoionization is adequately described by a one-electron model.

The single-electron picture seems to break down near 210 eV. The 3d asymmetry parameter experiences a resonance effect apparently associated with the onset of 3p ionization. Because this feature appears below the $3p_{3/2}$ ionization threshold at 214.4 eV, we assign this interchannel interaction as autoionization of a Rydberg level(s) involving excitation of a 3p electron. Three such levels have been observed in absorption,[14] the resonances at 210.7 eV ($3p \rightarrow 5s$) and 213.2 eV ($3p \rightarrow 6s,4d$) being the likely candidates for the effect observed here.

The intensity of the 3d̲4p̲np satellite peaks (underline refers to the hole states) relative to the 3d main line is shown in the top of Fig. 3. The $4p \rightarrow np$ satellites were unresolved in the TOF spectra: thus the results in Fig. 3 represent values for all of these peaks combined. Very little is known about the energy-dependent behavior of satellite intensities.[15] Empirically, Wuilleumier and Krause[16] have plotted satellite relative intensities against a reduced-energy parameter, ϵ/E_0, where ϵ is the kinetic energy of the satellite photoelectron, and E_0 is the satellite excitation energy (i.e. the binding energy of the satellite less the binding energy of the main line). For the Kr 3d̲4p̲np satellites, E_0 is approximately 20 eV, and the reduced-energy region covered by the measurements in Fig. 3 is

$3.5 \leq \epsilon/E_0 \leq 8.2$. At the upper end of this range, one suspects the high-energy or sudden limit to be reached.[16] Our high-energy value of 7.8(6)% agrees very well with an Al Kα measurement[17] of 8(1)% for the *sum* of the $4p \rightarrow np$ satellites. However, higher-resolution measurements with Mg Kα radiation[7] yielded 11.7% for these same transitions, which is in better agreement with the theoretical sudden-limit result[7] of 10.6%. Because the earlier measurements did not take the asymmetry parameter into account, they must be interpreted with caution. At lower energies we find the relative intensity to be larger than our high-energy value, illustrating that other processes besides shake-up may become important for lower values of the reduced energy. We note that the relative satellite intensity is decreasing in an energy range in which the 3d cross section is decreasing also [as determined from absorption measurements[18] and the fact that 3d subshell absorption dominates in this energy range (see Fig. 1)].

Even less is known about the energy dependence of satellite asymmetry parameters. As a first approximation, one might expect that the satellite β will mimic the asymmetry parameter of the main line. *Comparison of the 3d4pnp asymmetry parameter results in Fig. 3 to* β_{3d} (Fig. 2) shows that both β parameters increase in this energy range, but the slope for the satellite asymmetry parameter is about a factor of 2 larger than for β_{3d}. This intriguing result cannot be explained in the context of shake-up calculations.

For photon energies between 225 and 285 eV, evidence of 3p photoionization appeared in our spectra in the form of an $M_{2,3}M_{4,5}N$

Auger feature. These Auger transitions have been found to contribute approximately 50% to the decay of 3p vacancy states.[19] Consequently, we can estimate that 3p subshell absorption accounts for about 10% of the total absorption cross section in this energy range. The 3p photoemission peak itself was discernible for energies from 275 to 285 eV. The 3p asymmetry parameter was determined to be 0.26(8) in this range, lower than the HF-V result[10] of 0.5 at these energies. The measured value of β_{3p} is nearly the same as β_{3d} at the same photon energies. A similar result has been observed for the I 4p and 4d subshells in CH_3I.[4] In that work, recourse was made to strong many-electron interactions in the I 4p subshell in an attempt to understand this phenomenon. Ohno and Wendin[20] have discussed the same types of effects for the Kr 3p subshell. The asymmetry parameter for the $M_{2,3}M_{4,5}N$ Auger feature is 0.0(1). Likewise, the asymmetry parameters for the $M_{4,5}NN$ Auger peaks were found to be approximately zero over the energy range studied.

REFERENCES

*Work done in collaboration with P.H. Kobrin, C.M. Truesdale, P.A. Heimann, T.A. Ferrett, U. Becker, H.G. Kerkhoff, and D.A. Shirley

1. S.H. Southworth, P.H. Kobrin, C.M. Truesdale, D. Lindle, S. Owaki, and D.A. Shirley, Phys. Rev. A 24, 2257 (1981).

2. S. Southworth, U. Becker, C.M. Truesdale, P.H. Kobrin, D.W. Lindle, S. Owaki, and D.A. Shirley, Phys. Rev. A 28, 261 (1983).

3. P.H. Kobrin, P.A. Heimann, H.G. Kerkhoff, D.W. Lindle, C.M. Truesdale, T.A. Ferrett, U. Becker, and D.A. Shirley, Phys. Rev. A 27, 3031 (1983).

4. D.W. Lindle, P.H. Kobrin, C.M. Truesdale, T.A. Ferrett, P.A. Heimann, H.G. Kerkhoff, U. Becker, and D.A. Shirley (Chapter IV).

5. S.T. Manson and J.W. Cooper, Phys. Rev. 165, 126 (1968).

6. K. Siegbahn, C. Nordling, G. Johansson, J. Hedman, P.F. Hedén, K. Hamrin, U. Gelius, T. Bergmark, L.O. Werme, R. Manne, and Y. Baer, ESCA Applied to Free Molecules (North-Holland, Amsterdam, 1969).

7. D.J. Bristow, J.S. Tse, and G.M. Bancroft, Phys. Rev. A 25, 1 (1982).

8. M.O. Krause, Phys. Rev. 177, 151 (1969).

9. T.A. Carlson, M.O. Krause, F.A. Grimm, P.R. Keller, and J.W. Taylor, Chem. Phys. Lett. 87, 552 (1982).

10. D.J. Kennedy and S.T. Manson, Phys. Rev. A 5, 227 (1972).

11. K.-N. Huang, W.R. Johnson, and K.T. Cheng, At. Data Nucl. Data Tables 26, 33 (1981).

12. J.W. Cooper and S.T. Manson, Phys. Rev. 177, 157 (1969).

13. This effect is not a shape resonance, but simply the energy-dependent behavior of 3d photoionization into the $\ell=3$ continuum channel. This behavior is governed strongly by the centrifugal potential experienced by an ϵf continuum wavefunction at low kinetic energy. Related measurements that do involve shape resonances (potential barriers) can be found in Refs. 1-4.

14. W.S. Watson and F.J. Morgan, J. Phys. B 2, 277 (1969).

15. P.H. Kobrin, S. Southworth, C.M. Truesdale, D.W. Lindle, U. Becker, and D.A. Shirley, Phys. Rev. A 29 (1984); D.W. Lindle, T.A. Ferrett, U. Becker, P.H. Kobrin, C.M. Truesdale, H.G. Kerkhoff, and D.A. Shirley (Chapter VI), and references therein.

16. F. Wuilleumier and M.O. Krause, Phys. Rev. A 10, 242 (1974).

17. D.P. Spears, H.J. Fischbeck, and T.A. Carlson, Phys. Rev. A 9, 1603 (1974).

18. G.V. Marr and J.B. West, At. Data Nucl. Data Tables 18, 497 (1976); J.P. Connerade and M.W.D. Mansfield, Proc. R. Soc. Lond. A343, 415 (1975); A352, 557 (1977); J.B. West and G.V. Marr, ibid A349, 397 (1976).

19. M.O. Krause and T.A. Carlson, Phys. Rev. 149, 52 (1966).

20. M. Ohno and G. Wendin, J. Phys. B 11, 1557 (1978).

FIGURE CAPTIONS

Fig. 1. TOF photoelectron spectrum of Kr at a photon energy of 224 eV
and with $\theta=0^\circ$. All of the features below 60 eV are $M_{4,5}NN$
Auger lines. The 3d satellite includes all of the $4p \rightarrow np$
shake-up transitions. The peaks to the right of the 3d main
line arise from valence photoionization and from photoemission
induced by second- and higher-order components of the incident
radiation.

Fig. 2. Angular-distribution asymmetry parameter for Kr 3d
photoemission. Solid circles are the present results, open
circles and X's are from Refs. 9 and 8, respectively. The
solid and dashed curves are RRPA (Ref. 11) and HF-V (Ref. 10)
calculations, respectively. The RRPA curve has been shifted 9
eV to lower energy. The two calculations nearly coincide for
photon energies from threshold to 125 eV, at which point the
RRPA curve stops.

Fig. 3. Intensity relative to the 3d main line (top) and asymmetry
parameter (bottom) for the Kr 3d4pnp satellites. All of the
$4p \rightarrow np$ satellites were unresolved and are included in these
results.
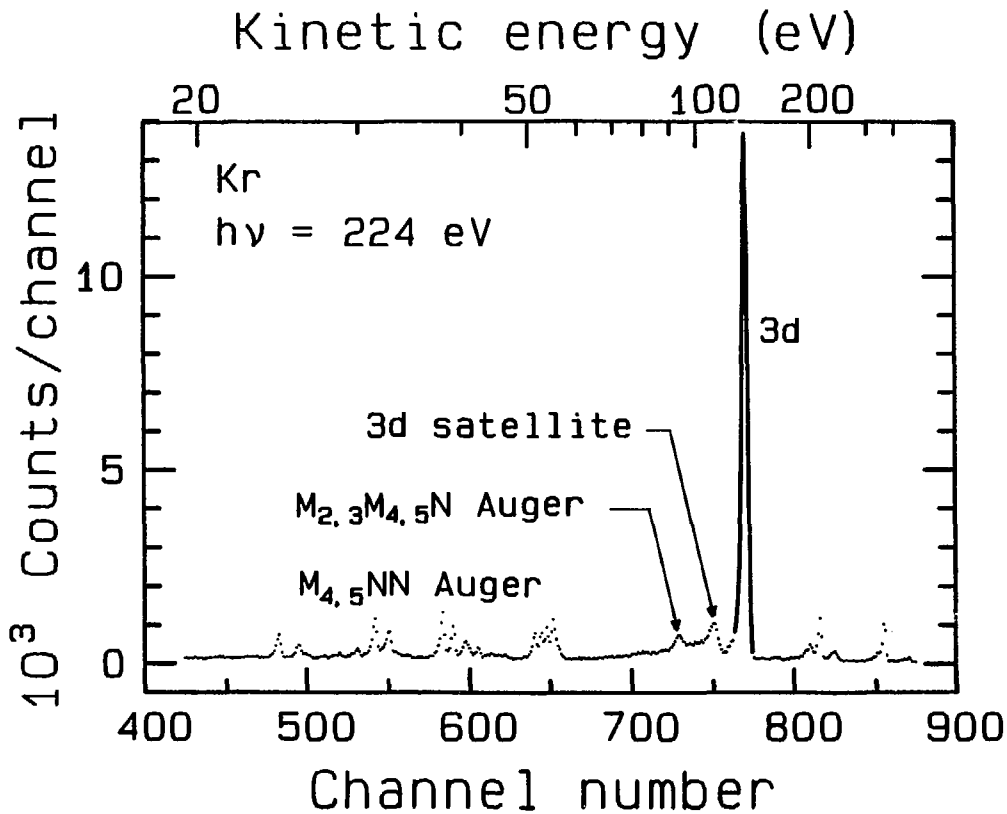
Figure 1

XBL 8311-4635
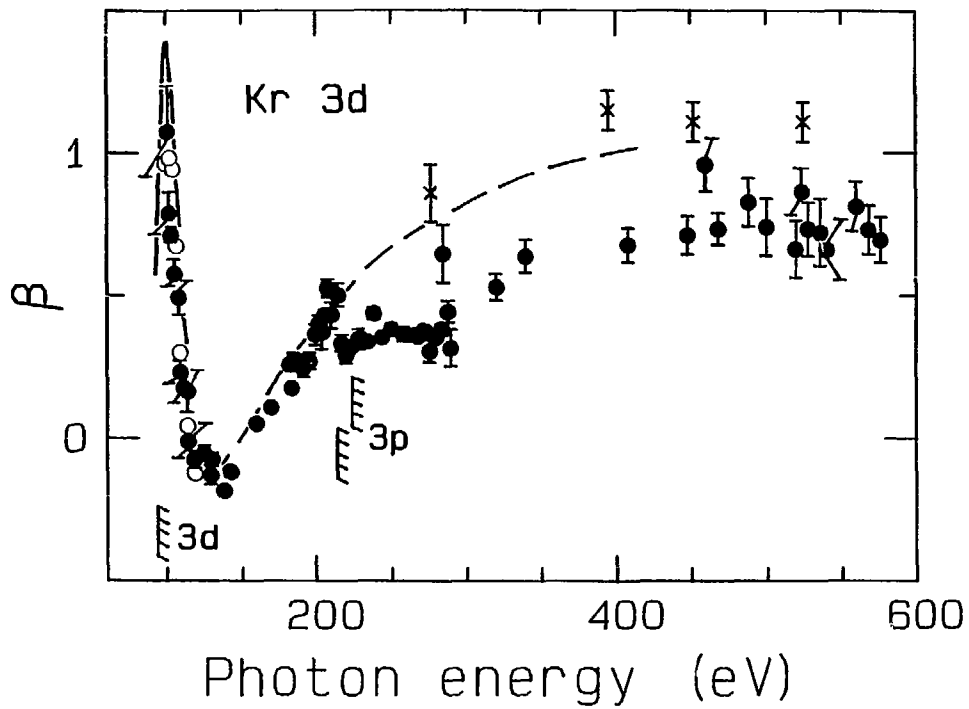
Figure 2

XBL 8311-4634
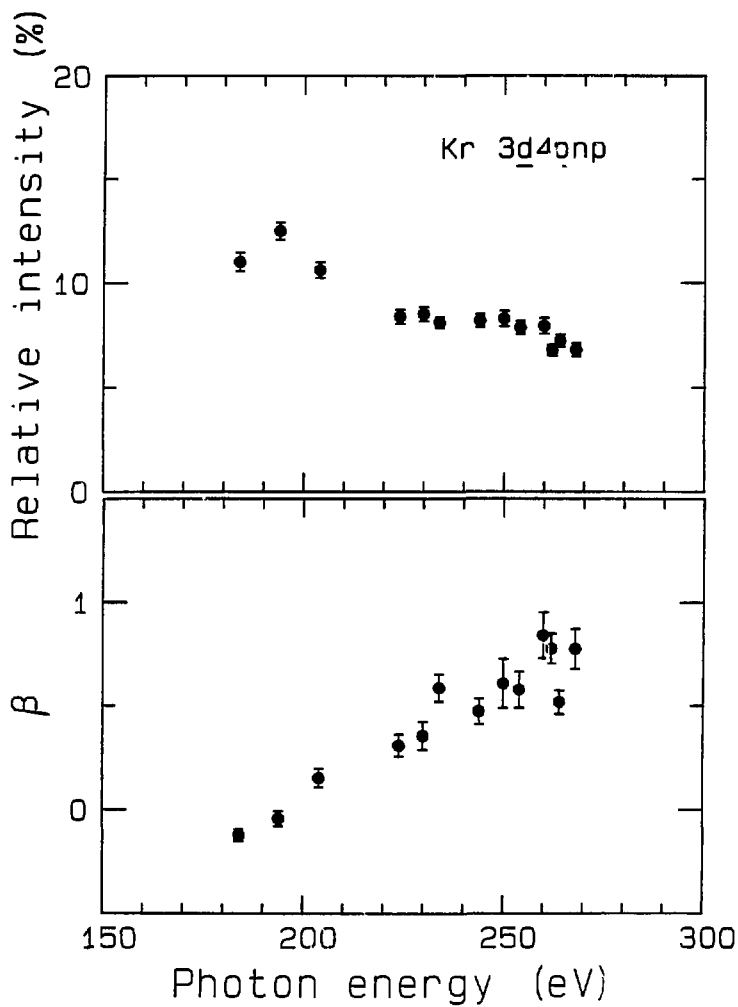
Figure 3

XBL 8311-4636

IV. INNER-SHELL PHOTOEMISSION FROM THE IODINE ATOM IN CH_3I*

A. INTRODUCTION

Recent photoelectron-spectroscopy (PES) studies of Xe[1-8] have highlighted both one-electron and multi-electron effects that are important in describing photoionization in the N and O shells of Xe above the 4d threshold. Elucidation of these effects has been accomplished by comparison of the experimental results to progressively more detailed theoretical calculations.[9-20] One result has been to identify Xe and other elements with similar Z as especially good systems for exhibiting some of these effects. The present photon-energy-dependent PES study of the iodine atom in CH_3I adds considerably to the available experimental measurements for elements near Xe in the periodic table.

For photon energies immediately above the 4d ionization threshold (Xe[7,8] or I), the photoelectron spectrum is dominated by features associated with 4d-vacancy states. It is known[7] that photoemission from the Xe 4d subshell can be described accurately by considering a series of single-electron effects that appear in the 4d → ϵf continuum channel; a Coulomb phase shift occurs near threshold, followed at somewhat higher energy by a shape resonance resulting from the trapping of the outgoing photoelectron by a centrifugal barrier, and finally at still higher energy, the 4d → ϵf dipole matrix element experiences a change in sign and causes a Cooper minimum. Experimen-

tally, pronounced changes corresponding to these phenomena have been seen in the subshell cross section,[2] the spin-orbit branching ratio,[4,5] and the angular distribution of Xe 4d photoelectrons.[3,7] To the extent that the iodine atom in a molecule such as CH_3I exhibits atomic-like behavior, the present measurements yield information about the Z dependence of the one-electron effects peculiar to $4d \rightarrow \epsilon f$ transitions. The present results indicate that the inner subshells of I in CH_3I are atomic-like. The I 4d subshell shows behavior remarkably similar to Xe 4d, with some small systematic variations. These results are discussed in Sect. B1.

Multi-electron effects generally become more important for the less intense (smaller cross section) features in photoelectron spectra. This is especially true for the '4p' shells of the elements in the series Te to Ba.[1,16] Quotation marks are used here because the final states that have binding energies in the vicinity of the 4p thresholds can be described adequately only in terms of collective effects;[16] hence designation as a 4p final state is inappropriate. In Xe for example, only one major discrete peak is observed in this energy range along with continuum-like structure,[1] contrary to the one-electron model prediction of two peaks corresponding to the $4p_{3/2}$ and $4p_{1/2}$ ionic states. The prominent peak has been attributed primarily to the $4d^8 4f$ configuration, and the remaining structure is explained in terms of the near-degeneracy of the 4p-vacancy states with $4d^8 n\ell$ singly-ionized and $4d^8$ doubly-ionized states.[16] As this near-degeneracy is enhanced (or removed) by observing different Z

elements, significant changes in the '4p' spectra are seen.[1] For I, the discrete structure is less intense than in Xe, and the identification of the single observed peak as a 4p-hole state is even more questionable. The cross section and angular distribution of the I '4p' peak as functions of photon energy are presented here for the first time (note that similar measurements have not yet been made for Xe '4p'). The asymmetry-parameter results are nearly identical to the I 4d results at the same photon energies. Though interpretation of these results is not straightforward, the assignment of the final state as $4d^84f$ is consistent with the results discussed in Sect. B2.

B. RESULTS AND DISCUSSION

A representative TOF photoelectron spectrum of CH_3I at a photon energy of 64 eV is shown in Fig. 1. The predominance in this spectrum of·features associated with I 4d ionization is apparent. The Auger peaks ($N_{4,5}VV$) result from the decay of the 4d-vacancy states. Both Auger features receive contributions from many decay channels, and no attempt is made here to assign any of these Auger transitions. The following subsections treat in turn each subshell from which we were able to detect photoelectrons; I 4d in Sect. B1 and I '4p' in Sect. B2.

1. I 4d SUBSHELL

Cross-section and asymmetry-parameter results for the I 4d

subshell are shown in Figs. 2 and 3. The I 4d cross section has been scaled to the absolute photoabsorption measurement of O'Sullivan[21] at the maximum in the cross section. The peak value in the absorption cross section is approximately 17 Mb. At certain photon-energy settings of the monochromator, a component of second-order radiation (i.e. an energy of $2h\nu$) was large enough to produce additional peaks in our spectra, primarily second-order peaks of I 4d photoelectrons. Because the β measurements are independent of the photon flux, we were able to use these spectra to extend our β_{4d} results to higher photon energies. The points obtained in this way are shown as open circles in Fig. 3.

The data in Figs. 2 and 3 are for the unresolved I 4d peak. Measurements in which the spin-orbit components, $4d_{5/2}$ and $4d_{3/2}$, are resolved at low kinetic energies are presented in Fig. 4. The binding energies of the $4d_{5/2}$ and $4d_{3/2}$ states are 56.7 and 58.3 eV, respectively.[21]

Interpretation of the results for the I 4d subshell benefits from the previous measurements[2-5,7,8] and calculations[9-13,17,19,20] for the Xe 4d subshell. The I 4d cross section shows two important effects. At 85-90 eV, the cross section reaches a maximum which can be attributed to a centrifugal-barrier shape-resonance effect in the $4d \rightarrow \epsilon f$ outgoing channel.[22] The position of the maximum agrees with the absorption measurement of O'Sullivan. The second effect occurs at 165-170 eV photon energy and can be assigned to a Cooper minimum[23] in the same $4d \rightarrow \epsilon f$ channel. Both of these phenomena in the I 4d

subshell occur at the same photoelectron energy (±5 eV) as in the Xe 4d case.[24-29] This concordance for the Cooper minima is based on comparison of the asymmetry-parameter data[7] because no measurements of the partial cross section at the Xe 4d Cooper minimum are available.

An atomic shape resonance is caused by a centrifugal barrier in the potential experienced by the ionized (or excited) electron. For energies below the peak of the barrier, the effect can be considered as a trapping of the electron. Typically, these barriers occur only for $\ell \rightarrow \ell'=\ell+1$ channels, in this case 4d $\rightarrow \epsilon f$, because the strength of the centrifugal repulsion scales as $\ell'(\ell'+1)$, where ℓ' is the orbital angular momentum of the electron in the final state. The nature of the barrier is sensitive to the interplay of the attractive Coulomb potential and the repulsive centrifugal potential. In a single-electron central-field model,[22] these potentials depend upon the values of Z and ℓ', respectively. Certain combinations of these parameters will produce centrifugal barriers; others will not.

When a barrier is present, the qualitative behavior of the cross section as a function of energy can be discerned from the following argument.[22] Considering only one-electron processes, the magnitude of the dipole matrix element that determines the single-channel cross section is proportional to the overlap between the initial bound one-electron wavefunction and the final continuum wavefunction. Near threshold, the centrifugal barrier excludes the continuum wavefunction from the interior of the atom and very little overlap occurs. As the available energy approaches the height of the barrier, the amplitude

for penetration of the continuum wavefunction into the interior of the atom increases quickly, causing a rapid increase of its overlap with the bound wavefunction. Accompanying this penetration is a phase shift of the continuum wave. These features constitute the shape resonance. At still higher energies the barrier plays a less important role, and the dipole matrix element gradually decreases with energy.

For $d \rightarrow \epsilon f$ transitions, the shape resonance is most pronounced for the elements in the periodic table centered around Xe,[22] because the 4f orbital has a high degree of continuum character in this sequence of atoms, so that virtual excitation to this orbital contributes significantly to the photoionization process.[30] This is apparently a general phenomenon. For the particular case of I $4d \rightarrow \epsilon f$, we are interested in the implications of the Z dependence of 4d cross sections. Compared to Xe, the centrifugal barrier in I is somewhat higher (Z is lower). This should cause the shape resonance to peak at a higher kinetic energy than in Xe. From a wavefunction overlap argument presented in Ref. 31, a second result of the higher barrier in I is to reduce the cross-section maximum compared to Xe.

Absorption measurements for the atomic species in the series Te,[32] I,[21,31,33-35] Xe[24,25,27-29] and Cs[33,36-38] (or molecules containing these atoms) imply a decrease of the kinetic energy of about 5 eV per series member for the shape-resonance maximum (approximately 40, 35, 30 and 25 eV, respectively). A photoemission measurement[2] of the Xe 4d cross section was consistent with the absorption result, but could not confirm it because of the scarcity of

data points. Likewise, the present measurement and another using electron energy-loss spectroscopy[39] are consistent with the photoabsorption peak measured for CH_3I^{21} (32 eV above threshold) and I_2^{31} (34 eV above threshold). However, our result also is consistent with the kinetic energy of the maximum in the Xe absorption[24,25,27] (30 eV) to within experimental error. We note the 2 eV difference between the peaks of the CH_3I and I_2 absorption results and suggest that it is due to molecular effects.

A definite minimum is observed in the I 4d cross section which falls to a value of ~0.1 Mb at 165-170 eV photon energy, then increases by a factor of 2 at higher energy. This minimum, which we interpret as a Cooper minimum arising from a sign change in the 4d → εf matrix element, occurs at the same kinetic energy (±5 eV) as the Cooper minimum in the Xe 4d subshell, as determined by comparison of the asymmetry-parameter results.[7] No other observations of Cooper minima in 4d subshell cross sections are available for further comparison.

The I 4d asymmetry-parameter results shown in Fig. 3 also are affected strongly by the shape-resonance and Cooper-minimum phenomena. The trapping of the outgoing photoelectron by the centrifugal barrier and the consequent phase shift are interpreted as causing the initial decrease in the measured 4d asymmetry. Because this happens before the barrier is overcome, the minimum in β_{4d} occurs at 15-20 eV lower kinetic energy than the maximum in the 4d cross section, or at approximately 70 eV photon energy.

Using the Cooper-Zare formula[40] for β in LS coupling, β_{4d} is predicted to be 0.1 at the Cooper minimum if spin-orbit and multi-electron effects are neglected.[41] This value for β_{4d} is reached at a photon energy between 165 and 170 eV, in complete agreement with the minimum in the cross-section results.

The theoretical curves[12,19,20] in Fig. 3 represent calculations for the Xe 4d subshell that have been shifted 11 eV to lower energy for comparison with the I 4d results at the same kinetic energy. A detailed comparison of these curves to experiment for Xe has been given in Ref. 7. Overall, the similarity between the I 4d and Xe 4d results (experimental and theoretical) is remarkable, especially in the region of the Cooper minimum which is predicted best by the relativistic random-phase approximation (RRPA)[20] and Dirac-Fock (DF)[19] calculations. At lower energies, around 70 and 150 eV, differences between the I 4d results and the Xe 4d predictions are more apparent. This observation can be understood in the light of the di⁻ ᵣₑ..ₑs between the shape resonances in Xe and I described above. ᵤompared to the experimental Xe 4d results, we note a general tendency for I β_{4d} to be less than Xe β_{4d} by 0.2-0.3 at all energies, a result for which we have no explanation. Near threshold, no experimental evidence for the predicted initial increase in I β_{4d} is seen, in agreement with the Xe 4d results.

One additional observation concerning the β_{4d} results pertains to the two points at 120 and 125 eV. Both of these points deviate significantly (by 0.3 or more) from a smooth curve connecting the

remainder of the data. Because of the proximity of the I '4p'
threshold at approximately 129 eV, we tentatively explain this
behavior as autoionization of Rydberg states leading to this threshold.
Clearly more experimental work with a finer mesh of points would be
needed to confirm this conjecture.

At the lowest photon energies used in this work, the spin-orbit
components of the I 4d peak were resolved (see Fig. 1). The $4d_{5/2}$-
to-$4d_{3/2}$ intensity ratio is shown in Fig. 4. It starts at 6 at 60.5
eV and quickly drops to the statistical value of 1.5. This behavior
is satisfactorily explained by a kinetic-energy effect; at a given
photon energy, the $4d_{5/2}$ peak has 1.6 eV higher kinetic energy than
the $4d_{3/2}$ peak, and thus is further along in its sharp increase in
cross section caused by the shape resonance (see Fig. 2). The
asymmetry parameters of the individual components are shown in the
bottom of Fig. 4. They follow the same trend as the unresolved β_{4d}
in Fig. 3. The differences between $\beta_{5/2}$ and $\beta_{3/2}$ also are
explained by the kinetic-energy effect.

An additional peak in the photoelectron spectra with a binding
energy of 72(1) eV appeared at photon energies from 110 to 130 eV.
This peak can be attributed to a correlation satellite(s) of the I 4d
main line. It probably corresponds to final states with a 4d vacancy
and a valence electron promoted from a nonbonding orbital localized on
the I atom ($E_{3/2}$ or $E_{1/2}$) to a higher-lying antibonding valence
orbital. The intensity of the satellite relative to the I 4d line is
15(4)% in this energy range. It appears strongly at these photon

energies probably because it experiences the same shape-resonance effect as the I 4d cross section.

2. I '4p' SUBSHELL

Svensson et al.[1] recorded Al Kα photoelectron spectra of the series of elements Te to Ba in the regions of their respective 4p binding energies. Rather than finding two peaks ($4p_{3/2}$ and $4p_{1/2}$) corresponding to single-electron transitions to the final state, each of these elements showed distinct multi-electron behavior to varying degrees; Te showing the largest effect, Ba the least. Wendin and Ohno[16] explained the situation for Xe in terms of strong many-electron effects that prevent the existence of an isolated $4p_{3/2}$- or $4p_{1/2}$-hole state, but require that a '4p' vacancy actually appears primarily as the Xe^{+} $4d^{8}4f$ state. This strong coupling results from the near-degeneracy of a single 4p hole and a double vacancy with two 4d holes. A similar description is based on the onset of energy-allowed $N_{2,3}N_{4,5}N_{4,5}$ super-Coster-Kronig decay in the range of Z from 52 (Te) to 56 (Ba).[16]

Because the TOF detectors record photoelectrons over a wide range of energies simultaneously, we obtained several spectra of the I '4p' region of CH_3I while making the measurements on the I 4d subshell. The '4p' spectra looked very similar to that of Svensson et al., and our measured binding energy of 129(1) eV agrees with theirs. The '4p' cross-section and asymmetry-parameter results for photon energies from

175 to 300 eV are shown in Fig. 5. These values were determined by considering only the area under the single prominent ($4d^8 4f$) peak and by excluding as much as possible the broad continuum-like structure at higher binding energy (see Fig. 5 of Ref. 1 for a spectrum of $CH_3 I$ in this region). We interpret the data in Fig. 5 as primarily representing the $4d^8 4f$ final state.

The I '4p' cross-section data in the top of Fig. 5 were scaled to the previously scaled I 4d cross section. The intensity of the $4d^8 4f$ peak accounts for only 25-50% of the total intensity in the '4p' binding-energy region. The remainder is contained in the broad continuum. Taking this extra intensity into account, the total I '4p' cross section is approximately equal to the I 4d cross section in this photon-energy range.

The I '4p' asymmetry-parameter results (Fig. 5) start at -0.3 at 175 eV, drop to a minimum of -0.6 at 190 eV and reach 0.5 by 300 eV. Included in Fig. 5 is one curve representing a Hartree-Fock velocity (HF-V) calculation[12] of Xe β_{4p}, shifted in energy to coincide with the I '4p' threshold, and a second derived from a smooth curve through the I β_{4d} data in Fig. 3. The HF-V curve, which predicts the behavior of β_{4p} in a single-electron approximation, does not agree with the data, whereas the latter curve fits the I β_{4p} results very well, suggesting the possibility of strong interchannel coupling between the 4d photoemission channels and the channels that lead to the '4p' peak. Interchannel coupling is plausible if the $4d^8 4f$ state reached via the '4p' transition is regarded as a multi-electron

satellite of the $4d^9$ final state. Identification of the exact mechanism by which these channels can couple through the continuum and lead to a β_{4p} similar to β_{4d} would require a more detailed theoretical model than any presently available.

C. CONCLUSIONS

Photon-energy-dependent measurements of the behavior of the I 4d and '4p' subshells in CH_3I have illustrated some important single-electron and multi-electron effects. The I 4d cross section and asymmetry parameter show pronounced changes under the influence of a shape resonance and a Cooper minimum in the $4d \rightarrow \epsilon f$ outgoing photo-electron channel. Analogous results have been observed for the Xe 4d subshell,[7] indicating not only the atomic-like nature of the I atom in CH_3I, but yielding useful information about the Z dependence of these one-electron effects on 4d-subshell ionization.

The first measurements as a function of photon energy for a '4p' subshell in the interesting elemental series Te-Ba have shown that interchannel coupling with the 4d channel strongly perturbs the '4p' asymmetry parameter. Still to be understood is the nature and relative composition of the final states other than $4d^8 4f$ contributing to the I '4p' peak, and how these states couple to the I 4d manifold to cause β_{4p} to be similar to β_{4d}. Further experimental studies on '4p' subshells in this region of the periodic table, especially Z=54 (Xe), are needed to aid in this understanding.

REFERENCES

*Work done in collaboration with P.H. Kobrin, C.M. Truesdale, T.A. Ferrett, P.A. Heimann, H.G. Kerkhoff, U. Becker, and D.A. Shirley

1. S. Svensson, N. Mårtennson, E. Basilier, P.Å. Malmquist, U. Gelius, and K. Siegbahn, Phys. Scripta 14, 141 (1976).

2. J.B. West, P.R. Woodruff, K. Codling, and R.G. Houlgate, J. Phys. B 9, 407 (1976).

3. L. Torop, J. Morton, and J.B. West, J. Phys. B 9, 2035 (1976).

4. S.P. Shannon, K. Codling, and J.B. West, J. Phys. B 10, 825 (1977).

5. M.S. Banna, M.O. Krause, and F. Wuilleumier, J. Phys. B 12, L125 (1979).

6. M.O. Krause, T.A. Carlson, and P.R. Woodruff, Phys. Rev. A 24, 1374 (1981).

7. S.H. Southworth, P.H. Kobrin, C.M. Truesdale, D. Lindle, S. Owaki, and D.A. Shirley, Phys. Rev. A 24, 2257 (1981).

8. S. Southworth, U. Becker, C.M. Truesdale, P.H. Kobrin, D.W. Lindle, S. Owaki, and D.A. Shirley, Phys. Rev. A 28, 261 (1983).

9. J.W. Cooper, Phys. Rev. Lett. 13, 762 (1964).

10. S.T. Manson and D.J. Kennedy, Chem. Phys. Lett. 7, 387 (1970).

11. S.T. Manson, Phys. Rev. Lett. 26, 219 (1971).

12. D.J. Kennedy and S.T. Manson, Phys. Rev. A 5, 227 (1972).

13. G. Wendin, J. Phys. B 6, 42 (1973).

14. M.Y. Amusia, N.B. Berezina, and L.V. Chernysheva, Phys. Lett. 51A, 101 (1975).

15. M.Y. Amusia and V.K. Ivanov, Phys. Lett. 59A, 194 (1976).

16. G. Wendin and M. Ohno, Phys. Scripta 14, 148 (1976).

17. W.R. Johnson and V. Radojević, J. Phys. B 11, L773 (1978).

18. M.Y. Amusia, Comments At. Mol. Phys. 8, 61 (1979).

19. W. Ong and S.T. Manson, Phys. Rev. A 21, 842 (1980).

20. K.-N. Huang, W.R. Johnson, and K.T. Cheng, At. Data Nucl. Data Tables 26, 33 (1981).

21. G. O'Sullivan, J. Phys. B 15, L327 (1982).

22. S.T. Manson and J.W. Cooper, Phys. Rev. 165, 126 (1968).

23. J.W. Cooper, Phys. Rev. 128, 681 (1962).

24. R. Haensel, G. Keitel, P. Schreiber, and C. Kunz, Phys. Rev. 188, 1375 (1969).

25. ⌐.L. Ederer and M. Manalis, J. Opt. Soc. Am. 65, 634 (1975).

26. A.P. Lukirskii, I.A. Brytov, and T.M. Zimkina, Opt. Spektrosk. 17, 438 (1964); [Opt. Spectrosc. 17, 234 (1964)].

27. D.L. Ederer, Phys. Rev. Lett. 13, 760 (1964).

28. T.M. Zimkina and S.A. Gribovskii, J. Phys. Coll. C4-10, 282 (1971).

29. J.P. Connerade, Proc. R. Soc. London, A347, 581 (1976).

30. For Z=56 (Ba), the 4f orbital is bound, but unoccupied, and very strong intershell-correlation effects related to the shape-resonance effects for lighter elements (eg. Xe, I) are important. See, for example; G. Wendin, J. Phys. B 9, L297 (1976); J.P. Connerade, Contemp. Phys. 19, 415 (1978) and references therein.

31. F.J. Comes, U. Nielsen, and W.H.E. Schwarz, J. Chem. Phys. 58, 2230 (1973).

32. T. Tuomi, B. Sonntag, and G. Zimmerer, DESY Report SR-72/14 (1972).

33. F.C. Brown, C. Gähwiller, H. Fujita, A.B. Kunz, W. Scheifley, and N. Carrera, Phys. Rev. B $\underline{2}$, 2126 (1970).

34. P.K. Carroll, E.T. Kennedy, and G. O'Sullivan, Appl. Opt. $\underline{19}$, 1454 (1980).

35. M. Pettini, M. Mazzoni, and G.P. Tozzi, Phys. Lett. $\underline{82A}$, 168 (1981).

36. M. Cardona, R. Haensel, D.W. Lynch, and B. Sonntag, Phys. Rev. B $\underline{2}$, 1117 (1970).

37. H. Petersen, K. Radler, B. Sonntag, and R. Haensel, J. Phys. B $\underline{8}$, 31 (1975).

38. K. Radler and B. Sonntag, Chem. Phys. Lett. $\underline{39}$, 371 (1976).

39. A.P. Hitchcock and C.E. Brion, J. Electron Spectrosc. $\underline{13}$, 193 (1978).

40. J. Cooper and R.N. Zare, J. Chem. Phys. $\underline{48}$, 942 (1968).

41. P.H. Kobrin, P.A. Heimann, H.G. Kerkhoff, D.W. Lindle, C.M. Truesdale, T.A. Ferrett, U. Becker, and D.A. Shirley, Phys. Rev. A $\underline{27}$, 3031 (1983).

FIGURE CAPTIONS

Fig. 1. TOF spectrum of CH_3I at 64 eV photon energy taken with the 54.7° analyzer.

Fig. 2. Partial cross section of the I 4d subshell in CH_3I, scaled at 85 eV to the absorption measurement of O'Sullivan, Ref. 21. These data represent the sum of the cross sections for the spin-orbit components, $4d_{5/2}$ and $4d_{3/2}$, with an average binding energy of 57.5 eV. The photon resolution for the measurements in this work is a constant 1.3 Å full-width at half maximum.

Fig. 3. Angular-distribution asymmetry parameter of the I 4d subshell in CH_3I. The data are weighted averages of the asymmetry parameters for the $4d_{5/2}$ and $4d_{3/2}$ final states. Solid and open circles represent data taken with first-order and second-order light, respectively. Theoretical calculations for the Xe 4d subshell shifted to coincide with the I 4d threshold; solid curves are Hartree-Fock length (HF-L) and velocity (HF-V) by Kennedy and Manson, Ref. 12; short-dashed curve is Dirac-Fock (DF) by Ong and Manson, Ref. 19; and long-dashed curve is relativistic random-phase approximation (RRPA) by Huang et al., Ref. 20.

Fig. 4. Branching ratio (top) and asymmetry parameters (bottom) for the spin-orbit components, $4d_{5/2}$ and $4d_{3/2}$. The point at 101.6 eV in the bottom panel represents β for both final states.

Fig. 5. Partial cross section (top) and asymmetry parameter (bottom)
for I '4p' photoelectrons from CH_3I [129(1) eV binding
energy]. The cross-section point at 250 eV has been excluded
because an Auger peak overlapped the '4p' peak in the TOF
spectrum at this photon energy. The curves in the bottom
panel represent HF-V calculations of Kennedy and Manson
(solid), Ref. 12, and a smooth curve (dashed) drawn through
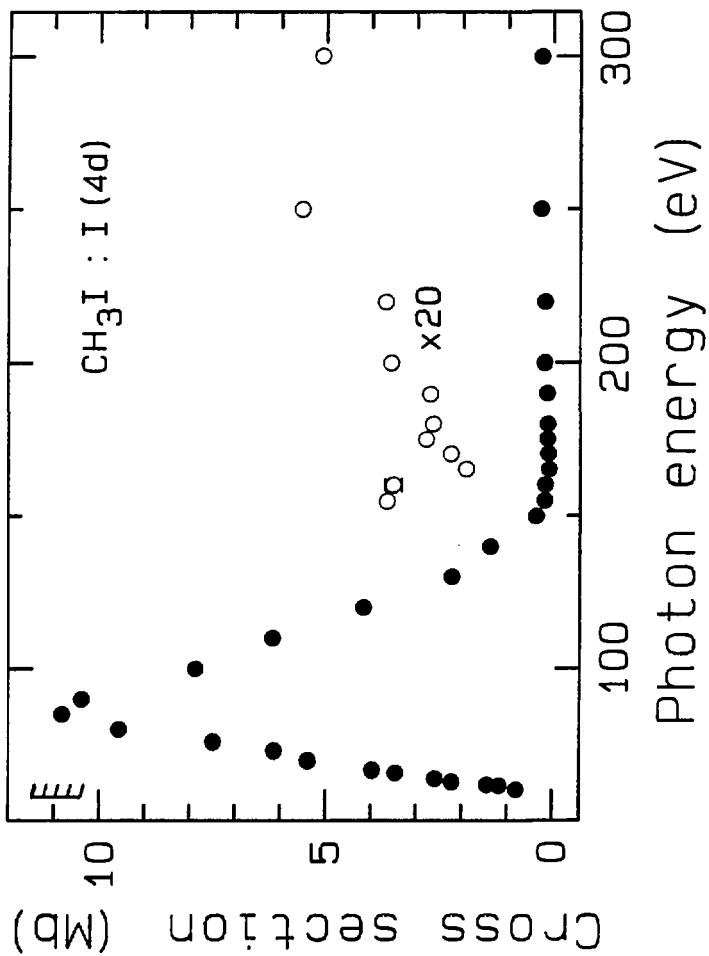the β_{4d} results in Fig. 3.

Figure 1

CH₃I : I (4d)
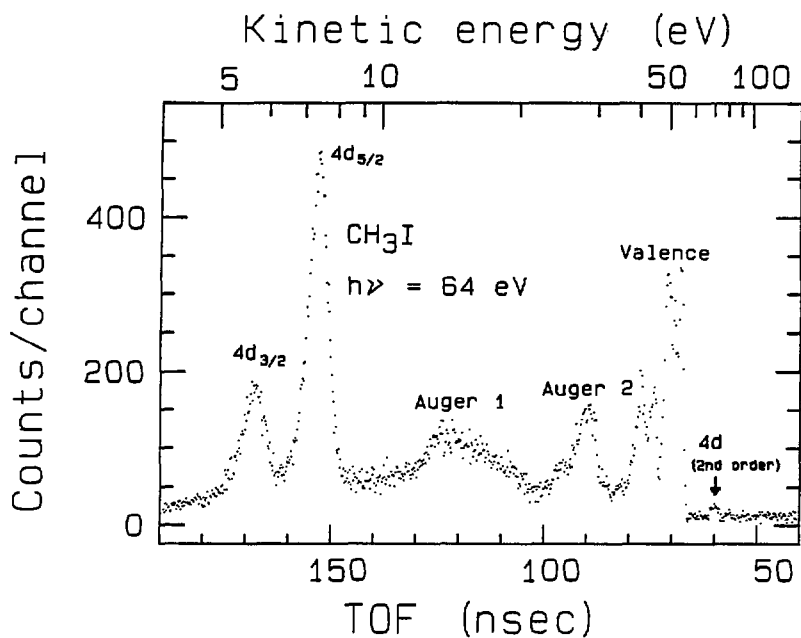
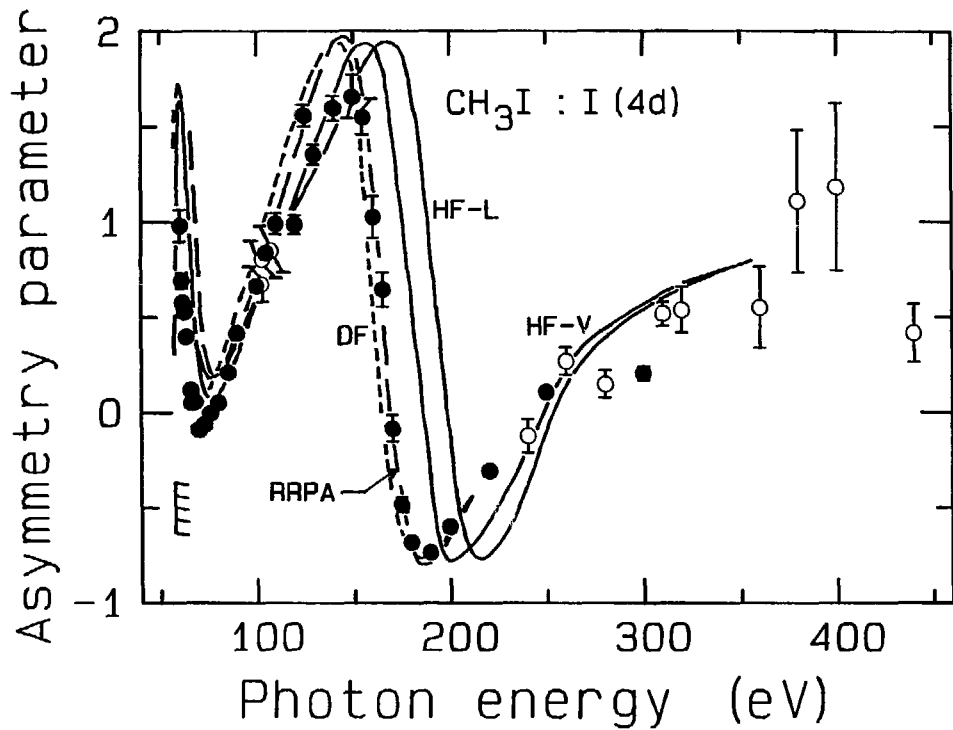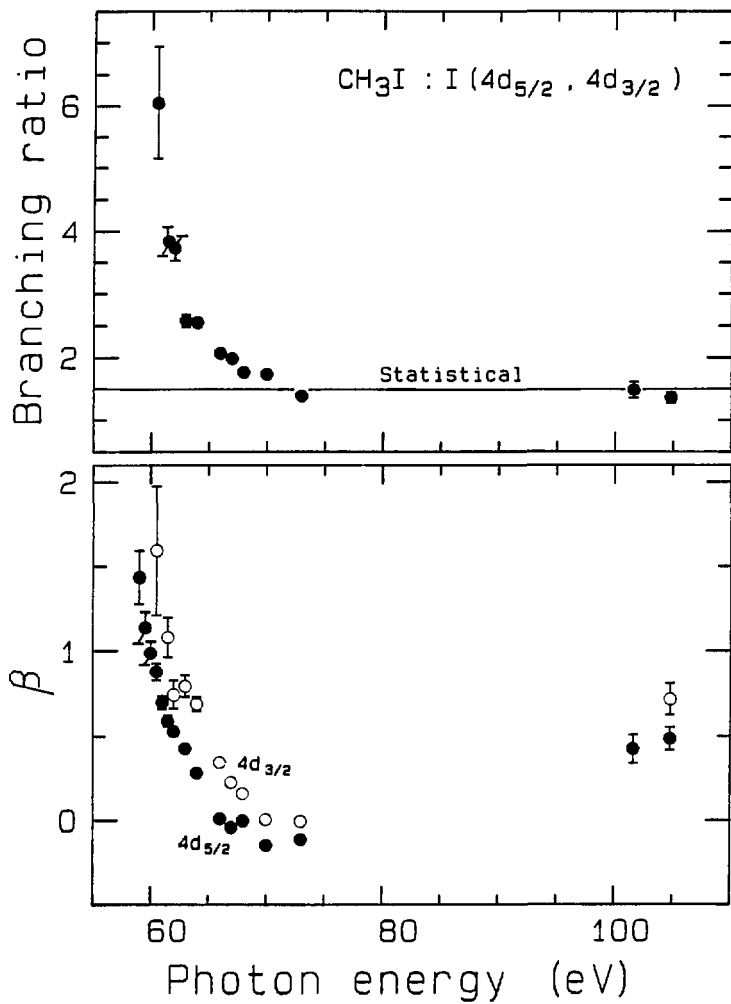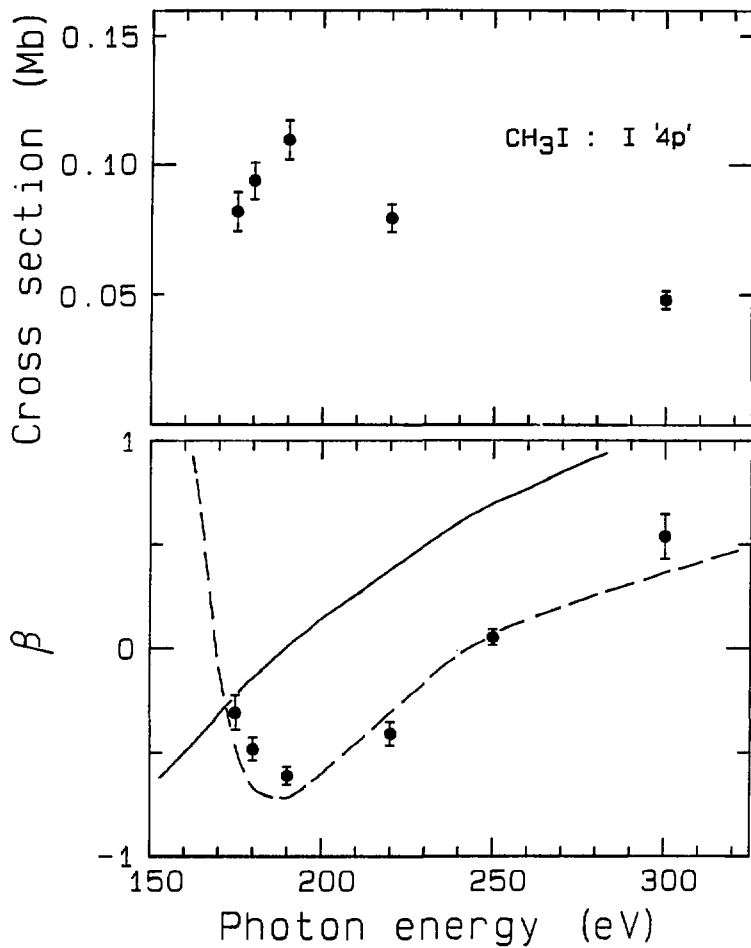XBL 836-10197

Figure 2

Figure 3

XBL 836-10198

Figure 4

XBL 836-10194

CH₃I : I '4p'

Figure 5

V. NITROGEN K-SHELL PHOTOEMISSION AND AUGER EMISSION FROM N_2 AND NO*

The process of molecular core-level photoionization, although initiated in localized regions near atomic nuclei, may exhibit intrinsically molecular effects because of the interaction of the photoelectron with the anisotropic molecular field.[1-3] One category of such effects arises from the shape of the molecular potential experienced by the photoelectron as it traverses from the interior to the exterior of the molecule: these effects therefore are referred to as 'shape resonances'.[4] Typically, a barrier of ~1-2 Ry is present in the potential, and it traps the photoelectron temporarily. This results in an enhancement of the photoionization cross section at an energy corresponding to the top of the barrier and a consequent change in the angular distribution of photoelectrons.[1-7]

The initial theoretical work on molecular shape resonances dealt with the K shell of N_2,[4] and the N_2 molecule continues to be of general interest in the theoretical[1-3,5-7] and experimental[8-18] study of shape resonances. However, experimental results for molecular core levels (i.e. excluding valence and inner-valence levels) have been restricted to absorption[8,11,13,15,16] and electron energy-loss[9,10,12,14,17,18] measurements, with the exception of three recent works that reported the use of photoelectron spectroscopy (PES) to study the C and O K shells,[19] the Si $L_{2,3}$ subshell,[20] and the Br $M_{4,5}$ subshell[21] in a few small molecules. The advantage of PES is its ability to measure photoelectron angular distributions, which

can be sensitive to the molecular potential and provide complementary information to a cross-section measurement. We report PES studies of the N K shell in both N_2 and NO. In addition, we report here N KVV Auger yields and angular distributions for N_2 in the interesting shape-resonance region.

A TOF spectrum of N_2 at 420 eV is shown in Fig. 1. The valence photoelectrons and the Auger electrons from the decay of N 1s vacancy-states are unresolved in all of the spectra. The spectra of NO have the same general appearance as the N_2 spectrum in Fig. 1. The photon energy of the monochromator was calibrated by measuring an excitation spectrum of the $1\sigma_u \rightarrow 1\pi_g$ ($2p\pi_g$ – referred to as $\pi*$) resonance in N_2 at 400.8 eV.[15,16] This also indicated a photon resolution of 2.5 eV for the N_2 results and 3.5 eV for the NO measurements.

Figure 2 shows the cross-section and asymmetry-parameter results for N 1s photoemission from N_2. The N 1s threshold in N_2 is 409.9 eV.[22] The cross-section data are normalized to the absorption measurement of Bianconi et al.[15] at 431.5 eV. Overall agreement with the absorption data is good, but the contrast ratio of the shape-resonance maximum at 419 eV is larger and the feature at 414 eV assigned as double excitation[12] is not as pronounced in the present data. The latter result is probably a consequence of the poorer photon resolution used in this work. Related electron energy-loss measurements[12,14,17] compare similarly to the present data and agree very well with the absorption results. Also shown with the cross-

section data are theoretical curves obtained with the multiple-scattering method (MSM)[4] and with Stieltjes-Tchebycheff moment theory (STMT).[6] Both calculations correctly predict the presence of a shape resonance arising from a centrifugal barrier in the $1\sigma_g \rightarrow k\sigma_u$ ($\ell=3$[5,6]) continuum channel. Quantitative agreement is better with the STMT calculation.

The N 1s asymmetry parameter in N_2, shown in the bottom of Fig. 2, is essentially constant from 414 to 418 eV, then rapidly increases to a high-energy asymptote near 2 by 440 eV. The proximity of the energy of the change in slope (418 eV) to the maximum in the cross section (419 eV) suggests that β is affected by the shape resonance. Qualitatively, this is borne out in the MSM calculations of Dill et al.[1] shown in the bottom of Fig. 2. Both the localized and delocalized curves indicate a minimum in β near the peak in the MSM curve for the cross section. However, the calculated changes are much larger than that observed. This may indicate that ground-state nuclear-vibrational effects in N_2 are significant for core-level shape-resonance phenomena.[23] Above 422 eV, presumably past the shape-resonance region, both curves agree well with experiment. The predicted and observed approaches to the high-energy asymptote of $\beta=2$ show that N 1s photoemission from N_2 becomes nearly atomic-like at high photoelectron energies. All of the N 1s results exhibit behavior similar to the C 1s measurements for the CO molecule,[19] which is isoelectronic with N_2.

The results for the N KVV Auger peak from N_2 are shown in Fig.

3. The data shown have been corrected for the valence photoelectron contribution that is unresolved from the Auger peak in the TOF spectra. The valence intensity and asymmetry parameter were estimated from spectra taken at photon energies below the discrete π^* resonance, where only valence ionization is energetically allowed. These values were assumed constant over the energy range of the measurements. The cross-section data were corrected by subtracting a constant background of approximately 0.2 Mb. This procedure did not change substantially the appearance of the data. On the other hand, the asymmetry-parameter correction was greatest at energies for which the Auger yield was lowest. The absolute corrections to β ranged from 0.0 to 0.3, all to lower values because of the relatively large β value (0.8) for the valence photoelectrons in this energy range. Interpretation of the asymmetry-parameter results must be made in light of this variable, and substantial, correction to the data.

The N KVV Auger yield from N_2, shown in the top of Fig. 3, has been normalized to the absorption measurement[15] at 431.5 eV. Agreement with the absorption results is very good; somewhat better than the agreement of the N 1s data. The broadening effect of the larger monochromator bandpass used in the present measurements is apparent in the π^* resonance profile at 400.8 eV. The MSM[4] and STMT[6] calculations are shown also for comparison, and we again note the better predictive abilities of the STMT approach.

In discussing the Auger asymmetry-parameter results, it is helpful to consider the formalism developed by Dill et al.[24] They

treat molecular K-shell photoionization and Auger decay as a two-step
process in which the angular distribution of the subsequent Auger
electrons depends explicitly on the alignment of the molecular ion.
As a result, the Auger asymmetry parameter β_A can be written

$$\beta_A(h\nu) = c\beta_m(h\nu) , \qquad (1)$$

where $\beta_m(h\nu)$ is an orientation parameter dependent on the alignment
produced by the initial photoionization event, and c is a constant
characteristic of each Auger decay channel. The values of $\beta_m(h\nu)$
and c are restricted to the ranges -1 to 2, and -1/2 to 1,
respectively. Note that all of the photon-energy dependence is
contained in $\beta_m(h\nu)$.

The Auger asymmetry-parameter results in the bottom of Fig. 3
represent weighted averages over all of the unresolved N_2 N KVV
transitions.[25,26] The β_A results can be divided into three groups;
the three points in the π^* resonance region, the data near threshold,
and the results above threshold (> 414 eV). The last group has an
average β_A of -0.05(4), consistent with an average value of zero
within systematic error. These results are compared in Fig. 3 to
$\beta_m(h\nu)$ from Dill et al.[24] The β_A data do show a systematic
curvature in this energy range, which may result from overestimation
of the valence contribution to the measured asymmetry parameter,
because the estimate was made at lower photon energies where the
valence cross section is larger. An explanation consistent with the
calculated curve for $\beta_m(h\nu)$ can be understood by noting that β_A

peaks at a photon energy of ~419 eV, slightly below the theoretical

peak of 421 eV for $\beta_m(h\nu)$. A shift in peak energy, together with a

greater width and smaller contrast ratio of the experimental maximum,

constituted the difference between experiment and theory for the N 1s

cross section. However, the experimental β_A data would have to be

shifted upward by about 0.2 in order for this "agreement" between β_A

and $\beta_m(h\nu)$ to be meaningful, because β_A and $\beta_m(h\nu)$ should be

related by the proportionality constant c that is independent of

photon energy. Further experiments with higher resolution would be

desirable to clarify this situation.

Several possible explanations could reconcile the difference

between the theoretical $\beta_m(h\nu)$ and the experimental β_A. Because

we measure β_A values averaged over all of the Auger transitions, it

is possible that the values of c for the different Auger channels

cause β_A to average to near zero at all energies. Another

possibility is that all or most of the c parameters are near zero.

Finally, the lack of agreement between the experimental and

theoretical results may bring into question the treatment of Auger

decay as a two-step process.

The β_A data near threshold show values slightly lower than the

results above threshold. Whether these values indicate Auger

asymmetries, as described by Dill et al.,[24] is unclear. Near

threshold, many Rydberg-like states are formed, but they are

unresolved in our measurements.

The results at the π^* resonance clearly indicate a nonzero value

of β_A. While it is certain from adsorbed-molecule experiments[27] and symmetry arguments that the $\pi*$-excited N_2 molecule is strongly oriented, the asymmetry of the autoionization electrons is quite small. The explanation[19] is probably that the excited electron remains as a "spectator", only weakly coupled to the decay process, thus retaining the total orientation of the molecule in the $\pi*$ orbital, while the subsequent electrons from an Auger-like decay show only an isotropic distribution, as would be required by angular-momentum conservation in the absence of strong coupling. The small, but nonzero, β_A may be understood from the observation[28] that a fraction of the autoionization decay from the $\pi*$ resonance in N_2 yields final states in which the excited electron did take part in the decay process. Previous measurements on the Ne K shell[29] and the C K shells of a few small molecules[19] have yielded similar results.

The results for N 1s photoemission from NO are presented in Fig. 4. There are two N 1s thresholds at 410.3 eV ($^3\Pi$) and 411.8 ($^1\Pi$).[22] We adopt an average binding energy of 411 eV for the unresolved N 1s peak in our work. Our cross-section results from N 1s photoemission have been scaled to the electron energy-loss measurements[30] for best agreement. Both sets of data exhibit the same general behavior, but the present results do not extend to low enough energy to observe the shape-resonance maximum at 414 eV.[30] Also shown is a MSM calculation[31] which predicts the maximum 4-5 eV too high and a contrast ratio much too large.

The NO N 1s asymmetry-parameter results in Fig. 4 show that the β

is low near threshold and rises rapidly to 2 by 425 eV. The predicted
minimum from the MSM calculations[3] is not apparent. The observed
shift of the measured β_{1s} values to lower energy by 4-5 eV with
respect to the theoretical results is consistent with the shift
observed for the N 1s cross-section maximum.

REFERENCES

*Work done in collaboration with C.M. Truesdale, P.H. Kobrin, T.A.
Ferrett, P.A. Heimann, U. Becker, H.G. Kerkhoff, and D.A. Shirley

1. D. Dill, S. Wallace, J. Siegel, and J.L. Dehmer, Phys. Rev. Lett.
   41, 1230 (1978); 42, 411 (1979).

2. J.L. Dehmer and D. Dill in Electron-Molecule and Photon-Molecule
   Collisions, ed. by T. Rescigno, V. McKoy, and B. Schneider (Plenum
   Press, New York, 1979).

3. S. Wallace, Ph.D. Thesis, Boston University (unpublished).

4. J.L. Dehmer and D. Dill, Phys. Rev. Lett. 35, 213 (1975).

5. J.L. Dehmer and D. Dill, J. Chem. Phys. 65, 5327 (1976).

6. T.N. Rescigno and P.W. Langhoff, Chem. Phys. Lett. 51, 65 (1977).

7. P.W. Langhoff in Electron-Molecule and Photon-Molecule Collisions,
   ed. by T. Rescigno, V. McKoy, and B. Schneider (Plenum Press, New
   York, 1979).

8. M. Nakamura, M. Sasanuma, S. Sato, M. Watanabe, H. Yamashita, Y.
   Iguchi, A. Ejiri, S. Nakai, S. Yamaguchi, T. Sagawa, Y. Nakai, and
   T. Oshio, Phys. Rev. 178, 80 (1969).

9. M.J. Van der Wiel, Th.M. El-Sherbini, and C.E. Brion, Chem. Phys.
   Lett. 7, 161 (1970).

10. M.J. Van der Wiel, and Th.M. El-Sherbini, Physica 59, 453 (1972).

11. A.S. Vinogradov, B. Schlarbaum, and T.M. Zimkina, Opt. Spectrosc.
    36, 383 (1974); [Opt. Spektrosk. 36, 658 (1974)].

12. G.R. Wight, C.E. Brion, and M.J. Van der Wiel, J. Electron
    Spectrosc. 1, 457 (1973).

13. A.S. Vinogradov, T.M. Zimkina, V.N. Akimov, and B. Schlarbaum, Izv. Akad. Nauk. SSSR, Fiz. Ser. 38, 508 (1974).

14. R.B. Kay, Ph.E. Van der Leeuw, and M.J. Van der Wiel, J. Phys. B 10, 2513 (1977).

15. A. Bianconi, H. Petersen, F.C. Brown, and R.Z. Bachrach, Phys. Rev. A 17, 1907 (1978).

16. H. Petersen, A. Bianconi, F.C. Brown, and R.Z. Bachrach, Chem. Phys. Lett. 58, 263 (1978).

17. A.P. Hitchcock and C.E. Brion, J. Electron Spectrosc. 18, 1 (1980).

18. M. Tronc, G.C. King, and F.H. Read, J. Phys. B 13, 999 (1980).

19. C.M. Truesdale, S.H. Southworth, P.H. Kobrin, U. Becker, D.W. Lindle, H.G. Kerkhoff, and D.A. Shirley, Phys. Rev. Lett. 50, 1265 (1983); C.M. Truesdale, D.W. Lindle, P.H. Kobrin, U.E. Becker, H.G. Kerkhoff, P.A. Heimann, T.A. Ferrett, and D.A. Shirley, J. Chem. Phys. (in press).

20. P.R. Keller, J.W. Taylor, F.A. Grimm, P. Senn, T.A. Carlson, and M.O. Krause, Chem. Phys. 74, 247 (1983).

21. T.A. Carlson, M.O. Krause, F.A. Grimm, P.R. Keller, and J.W. Taylor, Chem. Phys. Lett. 87, 552 (1982).

22. K. Siegbahn, C. Nordling, G. Johansson, J. Hedman, P.F. Hedén, K. Hamrin, U. Gelius, T. Bergmark, L.O.Werme, R. Manne, and Y. Baer, ESCA Applied to Free Molecules (North-Holland, Amsterdam, 1969).

23. J.L. Dehmer, D. Dill, and S. Wallace, Phys. Rev. Lett. 43, 1005 (1979).

24. D. Dill, J.R. Swanson, S. Wallace, and J.L. Dehmer, Phys. Rev.

Lett. $\underline{45}$, 1393 (1980).

25. T.A. Carlson, W.E. Moddeman, B.P. Pullen, and M.O. Krause, Chem. Phys. Lett. $\underline{5}$, 390 (1970).

26. W.E. Moddeman, T.A. Carlson, M.O. Krause, B.P. Pullen, W.E. Bull, and G.K. Schweitzer, J. Chem. Phys. $\underline{55}$, 2317 (1971).

27. J. Stöhr and R. Jaeger, Phys. Rev. B $\underline{26}$, 4111 (1982).

28. T.D. Thomas (private communication).

29. P.H. Kobrin, S. Southworth, C.M. Truesdale, D.W. Lindle, U. Becker, and D.A. Shirley, Phys. Rev. A $\underline{29}$ (1984).

30. G.R. Wight and C.E. Brion, J. Electron Spectrosc. $\underline{4}$, 313 (1974).

31. S. Wallace, D. Dill, and J.L Dehmer, J. Chem. Phys. $\underline{76}$, 1217 (1982).

FIGURE CAPTIONS

Fig. 1. TOF photoelectron spectrum of N_2 at 420 eV photon energy
taken with the $0^\bullet$ detector. The high-energy peak includes
both N KVV Auger electrons and valence photoelectrons.

Fig. 2. Cross-section (top) and asymmetry-parameter (bottom) results
for N 1s photoemission from N_2. The cross-section data have
been scaled to the absorption result (solid curve), Ref. 15, at
431.5 eV. Theoretical curves; top panel — MSM (short-dashed),
Ref. 4, STMT (long-dashed), Ref. 6; bottom panel — localized
(solid) and delocalized (dashed) MSM calculations, Ref. 1.

Fig. 3. Yield (top) and asymmetry parameter (bottom) for N KVV Auger
emission from N_2. The threshold for N 1s photoemission
(409.9 eV) has been indicated in both panels. The Auger-yield
data have been scaled as in Fig. 2. All of the cross-section
results above 405 eV have been multiplied by 5. The
theoretical curves in the top panel are the same as those in
the top panel of Fig. 2. In the bottom panel, the solid curve
is a calculation of $\beta_m(h\nu)$ using the MSM, Ref. 24.

Fig. 4. Cross-section (top) and asymmetry-parameter (bottom) results
for N 1s photoemission from NO. The cross-section data have
been scaled to the electron energy-loss results (solid curve),
Ref. 30, for best agreement, and both are in arbitrary units.
The dashed curve in the top panel is the MSM result, Ref. 31,
in Mb. The solid curve in the bottom panel is an MSM
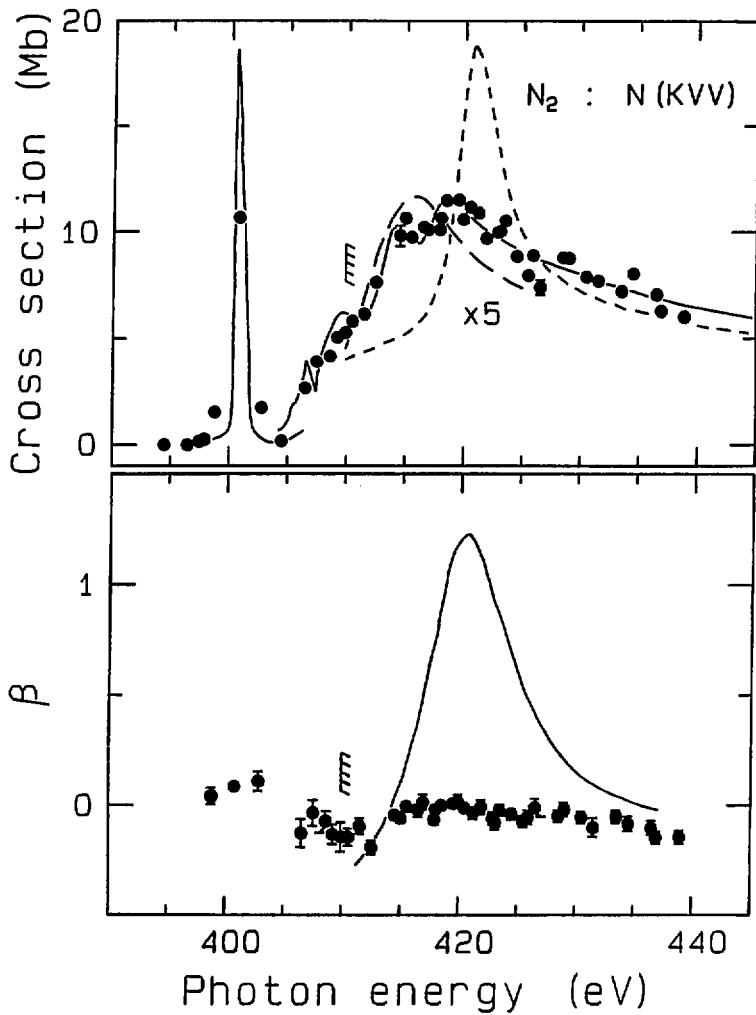calculation, Ref. 3.
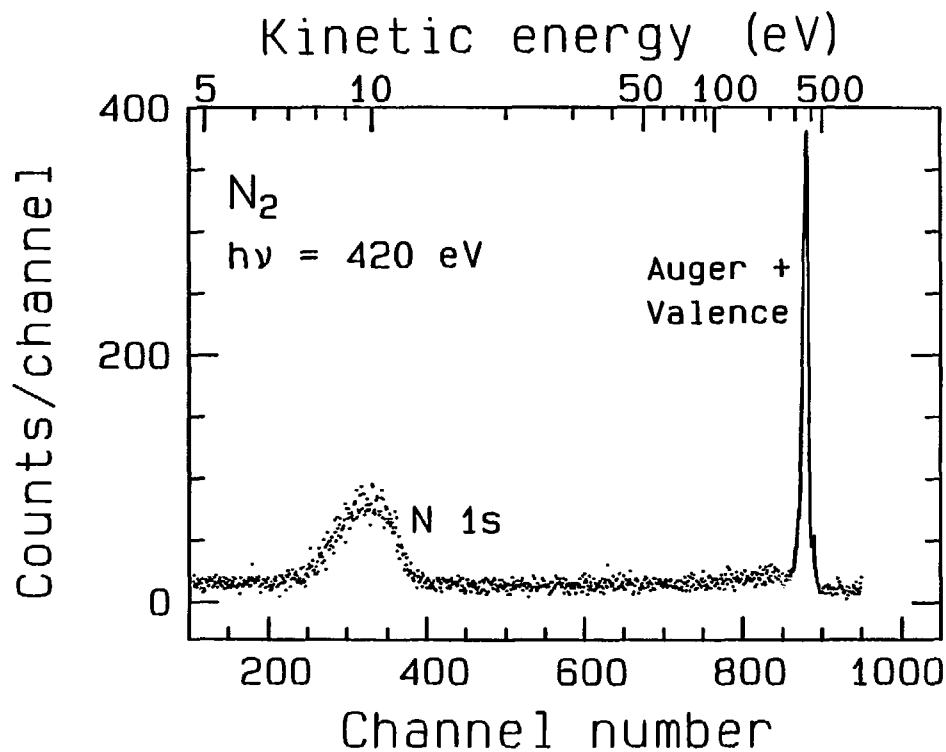
Figure 1

XBL 8310-12114

N_2 : N 1s
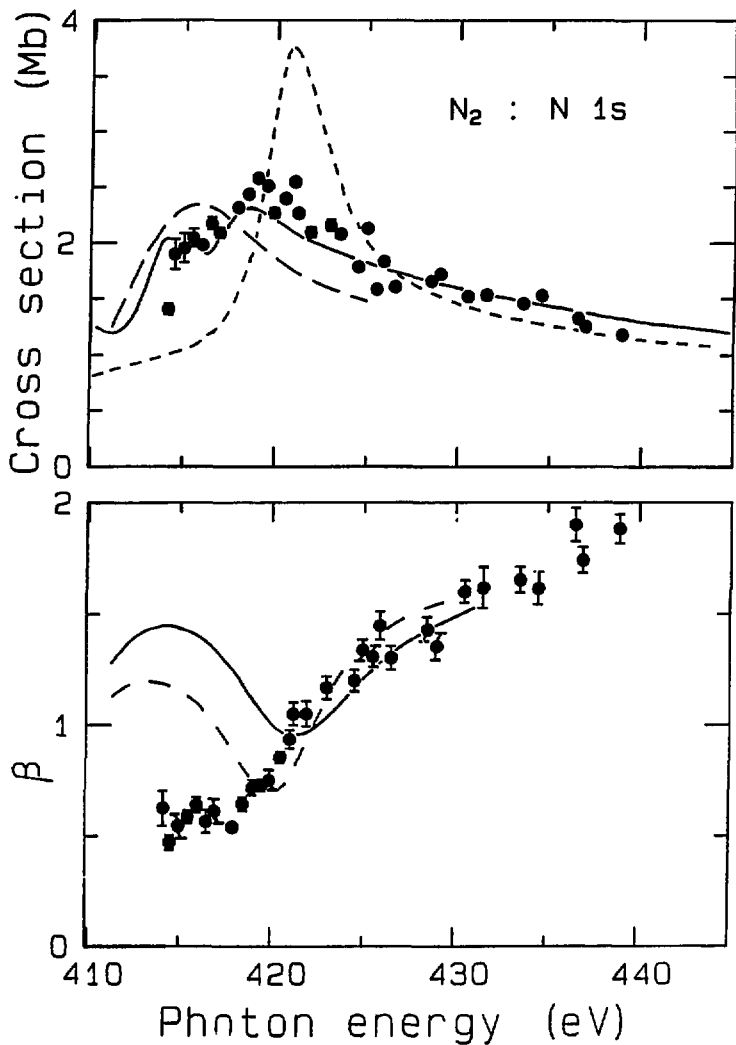
XBL 8310-12113

Figure 2

Figure 3
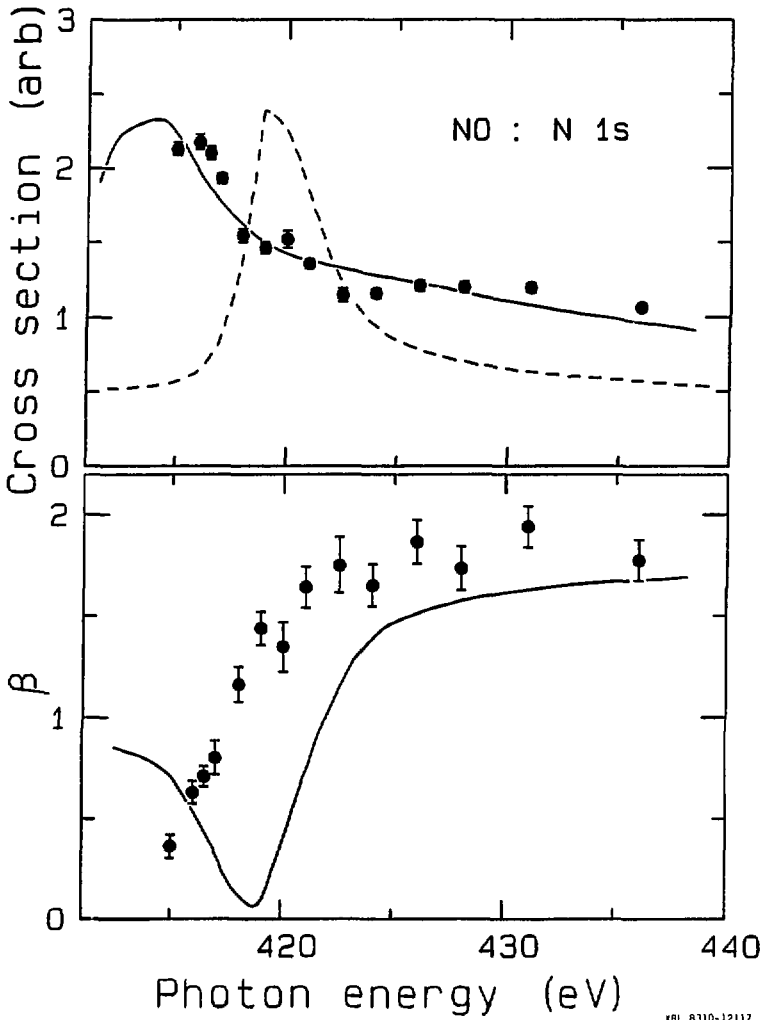
NO : N 1s

KBL 8310-12117

Figure 4

VI. PHOTOIONIZATION OF HELIUM ABOVE THE He$^+$(n=2) THRESHOLD:
AUTOIONIZATION AND FINAL-STATE SYMMETRY*

A. Introduction

The photoionization of helium provides the simplest example of electron correlation in atomic physics. Because correlation cannot occur in the hydrogen-like final state, theoretical studies of initial-state and continuum-state correlation effects are easier to interpret for the photoionization process. For this reason, helium is an important system for testing various theoretical approaches to the phenomenon of electron correlation. Past interest focused upon absolute cross-section measurements, as reviewed by Marr and West.[1] Theoretical calculations[2] of the total cross section, at least below the He$^+$(n=2) threshold, have proven to be very accurate. Recent interest[3-12] has centered upon the photoionization processes above this threshold, which can leave the residual He$^+$ ion in the 2s or 2p excited states. Several calculations[13-19] of the partial photoionization cross section, the satellite and subshell branching ratios, and the angular-distribution asymmetry parameter have been performed for the He$^+$(n=2) states, indicating that much is still to be learned from this simple system about the influence of correlation on measurable quantities.

Figure 1 depicts the atomic and ionic states in helium relevant to this experiment. We have studied the photoionization processes

$$He(1s^2) + h\nu \quad \rightarrow \quad He^+(1s,2s,2p) + e^- \tag{1}$$
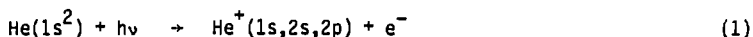
as a function of photon energy and photoelectron ejection angle. The $He^+(2s)$ and $He^+(2p)$ states are effectively degenerate in a photo-emission experiment, and thus comprise a single satellite line, which we designate $He^+(n=2)$. We have measured the partial cross sections, σ, and angular-distribution asymmetry parameters, β, for the processes represented in Eq. (1) that leave the He^+ ion in the 1s or the n=2 final states, as well as the branching ratio, $R_{21} = \sigma_{n=2}/\sigma_{1s}$, of the satellite intensity relative to that of the main line. The threshold for production of the n=2 states from the ground state of the helium atom is 65.4 eV. We have taken photoelectron spectra for photon energies from 1.9 eV above this threshold to 90 eV. This energy range can be divided into resonance and nonresonance regions. In the resonance region, it is possible to excite a series of Rydberg levels leading to the third ionization threshold at 73.0 eV, with subsequent autoionization.

The nonresonance data, taken with photon energies in the ranges 67.5 to 69.5 eV and 75 to 90 eV, show good agreement with previous measurements[4,6-8,10,12] and calculations[13-19] of the partial cross sections for both the n=1 and n=2 final states (processes DI in Fig. 1) and for the total (i.e. 2s plus 2p) satellite branching ratio. The ratio of the 2p cross section to the 2s cross section, R, which can be derived from $\beta_{n=2}$, provides a more sensitive test of theory. Discrepancies exist among the various experimental[9-12] and

theoretical[14-19] values of R reported to date. Chang[16] has predicted that near threshold the 2s contribution to $\sigma_{n=2}$ is larger than that of the 2p level, in contrast to several other predictions.[14,15,17-19] Experimentally, the earliest photoemission data[9] were consistent with either calculation, but later photo-emission[11,12] and fluorescence[10] measurements tended to discount Chang's prediction. Our results support the conclusion that the $He^+(n=2)$ final state is predominantly 2p near threshold. The disagreement in the theoretical results indicates the need for a better understanding of the contributions of electron correlation to the photoionization process.

A different perspective on correlation can be obtained in the analysis of autoionization resonances. The interaction of various continuum-state wavefunctions with an excited Rydberg level determines the extent and profile of the autoionization process. We have taken photoelectron spectra in the region of the lowest four Rydberg levels leading to the $He^+(n=3)$ ionization threshold at 73.0 eV. The four levels studied are indicated in the left-hand portion of Fig. 1. Large variations in $\sigma_{n=2}$ and $\beta_{n=2}$ were found at these resonances. Our measured variation in $\sigma_{n=2}$ agrees with the fluorescence data of Woodruff and Samson.[10] The detailed variation of $\beta_{n=2}$ over the autoionization resonances is presented here for the first time. In addition, we infer from our measurements that the shape of the total cross section over the first member of this Rydberg series differs with earlier experimental[20] and theoretical[21,22] results, but is

consistent with recent photoemission data.[12]

An example of a time-of-flight spectrum for helium from the 54.7° detector is shown in Fig. 2. The nonresonance data are presented in Section B, and the behavior of the cross sections, branching ratios and asymmetry parameters over the autoionization resonances is discussed in Section C. Conclusions are presented in Section D.

B. NONRESONANCE PHOTOIONIZATION

Our measurement of the branching ratio R_{21} is shown in Fig. 3 along with several theoretical curves and other experimental measurements. The present results show excellent agreement with the previous measurements.[4,5,8] We see also that the available theoretical calculations[13-17] agree reasonably well with one another and predict the branching ratio to within ~25%. The absolute partial cross section of the n=2 satellite is also predicted well by these same calculations. We do not show our relative partial cross sections for the n=2 or 1s levels, but note that they also agree with the previous measurements.

The ability to predict the energy dependence of R_{21} appears to be nearly independent of the degree of configuration interaction (CI) included in the calculations, but this is not true when the individual partial cross sections for the 2s and 2p final states are considered. The measurement of these partial cross sections, or their ratio, is a more sensitive test of the theoretical calculations, because the energy dependences of σ_{2s} and σ_{2p} are quite different. The reasons

for these differences can be understood from a discussion of CI as it
pertains to helium photoionization.

For the case that CI is only important in the initial (eigen)
state of the helium atom (ISCI), the initial state is written properly
as an admixture of the $1s^2$, 1s2s, $2s^2$, $2p^2$, and higher configurations.
The ground state is predominantly $1s^2$. If we consider then that the
$1s^2$, 1s2s, $2s^2$, $2p^2$, etc. configurations are not eigenstates
(i.e. they are not orthogonal to each other), then the degree to which
any one of the other configurations mixes into the ground state can be
estimated by considering its overlap with the $1s^2$ configuration.[23]
This estimate suggests that 1s2s and $2s^2$ play a more important role
in ISCI than does $2p^2$. Furthermore, if we assume that the partial
cross sections for the production of the 2s and 2p final states (by
ionization from the 1s2s, $2s^2$, or $2p^2$ configurations) are dependent
only on the mixing coefficients of 1s2s, $2s^2$, and $2p^2$ in the
initial state, then we expect ISCI to lead to a predominance of
$He^+(2s)$. We also can see that this result is valid for all photo-
electron energies because the ISCI mixing coefficients are independent
of energy. Thus, if CI were to occur only in the initial state, the
ratio R would be constant and probably less than unity.

However, the effects of CI in the continuum state (CSCI) must
also be considered. The continuum state includes both the ionic core
left after photoionization and the photoelectron. For simplicity in
this discussion, we will consider the initial state to be completely
$1s^2$. Configuration interaction in the continuum thus constitutes

mixing of configurations such as 2sεp and 2pεs with 1sεp. Again, we estimate the degree of mixing by examining the overlap of a given configuration with 1sεp. Because the photoelectron is included in these wavefunctions, we can expect the mixing coefficients, and hence the 2s and 2p cross sections, to be energy dependent. Because of the nature of continuum wavefunctions at low energy, the overlap between 2pεs and 1sεp is largest near threshold, diminishing with increasing energy.[23] The overlap between 2sεp and 1sεp will be less energy dependent, because of the similarity of the continuum part of these two configurations. The result of CSCI would then likely be a predominance of the 2p final state near threshold, this predominance decreasing as the energy increases. This discussion of CSCI is over-simplified to the extent that we have ignored the near degeneracy of the 2s and 2p final states. Their proximity in energy allows them to be strongly coupled in the continuum state. Despite this complication, we expect the conclusions to be qualitatively correct.[23]

To understand the complete picture for helium photoionization, it is necessary to combine the effects of ISCI and CSCI discussed above. Configuration interaction in the hydrogen-like final state is not possible, and does not need to be considered. Qualitatively, we conclude that at threshold the 2p final state will be maximally produced and may be more likely than the 2s final state, whereas in the high-energy limit, the 2s final state will be most important. Similar conclusions can be derived from a different argument using shake theory.[17] Quantitatively, the degree of predominance of one

final state over the other and the applicable energy ranges can only be determined by theoretical calculations that accurately treat the effects of ISCI and CSCI. Comparison of such calculations with experimental results can yield information about the type and degree of CI present in the helium system, as well as important results concerning what treatments of CI are most accurate.

Experimentally, two approaches have been taken. Woodruff and Samson[10] measured R directly by taking advantage of the long lifetime of $He^+(2s)$ to distinguish between fluorescence from the 2s and 2p levels. A second method, used by several groups,[9,11,12] including ours, relies on the measurement of the asymmetry parameter, $\beta_{n=2}$, which is a weighted average of β_{2s} and β_{2p}:

$$\beta_{n=2} = \frac{\sigma_{2s}\beta_{2s} + \sigma_{2p}\beta_{2p}}{\sigma_{2s} + \sigma_{2p}} \quad . \tag{2}$$

By rearranging Eq. (2), and assuming that β_{2s} is always 2, R can be expressed in terms of $\beta_{n=2}$:

$$R = \frac{\sigma_{2p}}{\sigma_{2s}} = \frac{2 - \beta_{n=2}}{\beta_{n=2} - \beta_{2p}} \quad . \tag{3}$$

This latter approach of course, must rely on the calculated values of β_{2p}. Fortunately, the two available calculations[9,15] of β_{2p} agree rather well.

Our results for $\beta_{n=2}$ are presented in Fig. 4 along with the other experimental results[9,11,12] for $\beta_{n=2}$ and theoretical

calculations[9,15] of $\beta_{n=2}$ and β_{2p}. Agreement among the experiments is excellent throughout the energy range shown. The region between 70 and 75 eV is blank because of the presence of several strong auto-ionizing resonances (see Section C). Figure 5 shows the values of R derived from the experimental data in Fig. 4 and the calculated values of β_{2p} from Jacobs and Burke.[15] Also shown are five calculations[14-19] of this ratio and the direct measurements of R by Woodruff and Samson.

The strong energy dependence of R below 100 eV can be understood from the above discussion of ISCI and CSCI. Because CSCI is more important at lower energies, we expect σ_{2p} to make a stronger contribution to $\sigma_{n=2}$ near threshold, as confirmed by the data. Also, since ISCI is nearly energy-independent, we expect the ratio σ_{2s}/σ_{1s} to be fairly constant for all photon energies. Direct measurements[10] of σ_{2s} support this conclusion for the first 60 eV above the 2s threshold. At the high-energy limit the n=2 peak should be mostly 2s,[23] though no experimental confirmation is available. The satellite branching ratio, R_{21}, in this limit has been calculated[13,15] to be 4.8%, which can be compared to the values of 6(1)% at 190[6] and 278 eV[3] photon energy and 5.0(8)% for an Al Kα measurement.[5]

The theories used in the calculation of R differ significantly in sophistication. The calculation of Richards and Larkins[17,19] used Hartree-Fock (HF) wavefunctions in which the effects of relaxation have been included, but not CI. The calculation by Chang[16] also

used HF wavefunctions, but included CI in both the initial state and the continuum states. Jacobs[14] and Jacobs and Burke[15] used a 56-term Hylleras initial-state wavefunction, which is a nearly exact approximation of the $He(1s^2)$ ground state, and a close-coupling calculation for the final state, which is similar to CSCI. The calculation by Berrington et al.[18] is an improvement on the earlier close-coupling calculations in which care was taken to use the same configurations in the expansions for both the initial and continuum states. All of the calculations used final-state wavefunctions that are purely hydrogenic.

Above 85 eV, all of the calculations show the same behavior and they all agree with experiment to within the errors. Below 85 eV, however, Chang's curve deviates significantly from the rest and predicts a predominance of 2s near threshold. The experimental results show clearly that this is not correct, and we conclude that the 2p final state is the major component of $He^+(n=2)$ at threshold, being more than twice as likely as the 2s final state. The calculation of Berrington et al. shows the best overall agreement with the present results.

The three close-coupling calculations (Jacobs, Jacobs and Burke and Berrington et al.) and the calculation of Richards and Larkins behave similarly at low energy, despite the fact that the latter is a much less sophisticated calculation. Richards and Larkins have concluded that CI and exchange are unimportant to their calculation except near threshold, and they cite this as the reason their

calculation does so well. Furthermore, they suggest[24] that the discrepancy in Chang's calculation may be the result of the use of CI wavefunctions that do not accurately take into account the direct interaction of the outgoing channels, which the other calculations do.[14,15,18] This ultimately may be the result of cancellation between large terms in the calculation of the transition amplitude.[16]

This example illustrates that much is still to be learned about the effects of CI on the calculation of the energy dependence of satellite cross sections. Except for isolated calculations on the Ne K shell,[25] the Li K shell,[17,19] and the valence shell of Fe,[26] the helium calculations are the only such theoretical studies completed to date. Helium thus appears to be a good candidate for further studies of electron-correlation effects in atomic photoionization.

At the photon energy of 80 eV (see Fig. 2), we were able to detect photoelectrons from the $He^+(n=3)$ final state. We determine its branching ratio relative to the main line, R_{31}, to be 1.8(2)% and its asymmetry parameter to be -0.2(2). This value for R_{31} is in agreement with previous estimates[8,17,27] at this energy and the data of Bizau et al.[28] It also can be compared to the Al $K\alpha$ result of 1.4(8)%.[5] The negative value for $\beta_{n=3}$ indicates that the 3s final state is not the major component of this peak. In fact, the result of -0.2(2) is consistent with the threshold value of -0.04 calculated by Greene,[29] who found approximately equal contributions from 3s, 3p, and 3d.[30]

C. RESONANCE PHOTOIONIZATION

Madden and Codling[31] first observed the Rydberg levels leading to the n=3 ionization threshold in helium in the energy range $69.5 \leq h\nu \leq 73.0$ eV. Of the five possible Rydberg series in this region, only one has been found to be significant. It is designated (sp, 3n+) $^1P^\bullet$, which is a positive admixture of 3snp $^1P^\bullet$ and 3pns $^1P^\bullet$. It has also been given[32] the notation 1_n, which we shall use here except when the 1_3 resonance is discussed alone: then we shall refer to it as the 3s3p resonance. The (sp, 3n-) $^1P^\bullet$ (or -1_n) series, the negative admixture of 3snp $^1P^\bullet$ and 3pns $^1P^\bullet$, has also been observed, but it is small enough to be neglected in the present analysis. The other possible $^1P^\bullet$ series (with major component 3pnd, 3dnp or 3dnf) have not been observed.

The remainder of this section will deal with the analysis of the cross-section, branching-ratio, and asymmetry-parameter profiles over the 1_n series of resonances. To lay the groundwork for this analysis, we begin (Sect. C1) with a summary of several formalisms for describing autoionization phenomena. How these formalisms are used to fit the satellite data is discussed in Sect. C2. Quantitative results for the cross section and branching ratio of the n=2 satellite are presented in Sect C3. From these results, we have inferred qualitative information about the resonance profiles of σ_{1s} and the total cross section, σ_t. Resonance parameters are presented for σ_{1s} and σ_t with the proviso that the quantitative results may not be very

accurate, but are given to illustrate the usefulness of this type of analysis. To this end, we determine several other parameters, including individual dipole matrix elements, to illustrate methods for the quantitative interpretation of an autoionization process. In Sect. C4, the $\beta_{n=2}$ resonance profile is discussed quantitatively, and inferences for the ratio R in the resonance region are made.

1. THEORETICAL BACKGROUND

The effect of an isolated resonance, such as a Rydberg level, on the total photoabsorption or total photoionization cross section was derived originally by Fano.[33] The presence of a discrete level embedded in one or more continua causes an interference in the photon absorption process because of the indistinguishability of the two pathways, direct ionization and autoionization, leading to the final state. Fano derived the following expression for the total cross section, σ_t, for the case of a single discrete state interacting with one or more continuum states:

$$\sigma_t = \sigma_0 \left[\rho^2 \frac{(q + \varepsilon)^2}{1 + \varepsilon^2} + 1 - \rho^2 \right] , \tag{4a}$$

$$\varepsilon = \frac{E - E_0}{\Gamma/2} , \tag{4b}$$

where the Fano parameters q and ρ^2 are assumed constant over the

resonance, σ_0 is the cross section far from the resonance, Γ and E_0 are the full-width at half maximum (FWHM) and the position of the resonance, respectively, and ϵ is a reduced energy.

The quantities q, ρ^2, σ_0 and Γ all can be expressed in terms of the dipole matrix elements for transitions from the ground state, g, to the discrete state, ϕ, and to the continua, μ, together with the Coulomb-interaction matrix elements coupling the discrete state to the continua. The q parameter, which governs the shape of the total cross section, is given by

$$q = \frac{\langle\phi|\vec{r}|g\rangle}{\pi \sum_\mu \langle\phi|V|\mu\rangle\langle\mu|\vec{r}|g\rangle} \quad , \tag{5}$$

and the correlation coefficient, ρ^2, which is a measure of the strength of the resonance, is given by

$$\rho^2 = \frac{\sum_\mu |\langle\phi|V|\mu\rangle\langle\mu|\vec{r}|g\rangle|^2}{\sum_\mu |\langle\phi|V|\mu\rangle|^2 \sum_\mu |\langle\mu|\vec{r}|g\rangle|^2} \quad , \tag{6}$$

where $\vec{r}$ and V represent the dipole and Coulomb operators, respectively, and Φ is the discrete state modified by an admixture of the continuum states. The degree to which Φ is different from ϕ is dependent upon the energy variations of the continuum wavefunctions in the vicinity of the resonance. The linewidth of the resonance is given by

$$\Gamma = 2\pi \sum_\mu |\langle \phi|V|\mu\rangle|^2 \quad , \tag{7}$$

and the nonresonance, background cross section is given by

$$\sigma_0 = \sum_\mu |\langle \mu|\vec{r}|g\rangle|^2 \quad . \tag{8}$$

While the matrix elements in Eqs. (5) and (6) are not strictly energy-independent, they are slowly-varying functions of energy, and q and ρ^2 are therefore assumed to be constant in the vicinity of the resonance.

The Fano parametrization [Eqs. (4)-(8)] can explain the many different shapes measured for autoionization resonances. For example, the sign of the q parameter determines whether the resonance profile of the total cross section reaches its minimum on the low-energy side (q > 0) or the high-energy side (q < 0) of the resonance. This property will be referred to as the 'phase' of the resonance profile. Other shapes can also be obtained from these expressions, such as a window resonance (q = 0) or a noninterfering Lorentzian peak added to the background cross section (|q| >> 0).

The parametrization shown above is most applicable to the effect of an isolated resonance on the total photoabsorption cross section. In general, however, atomic Rydberg levels form a series whose members are not well-separated in energy and thus cannot be considered isolated. Equation (4a) is not easily adaptable to such a series of noninteracting, closely-spaced resonances because the background cross

section appears as a multiplicative factor for each resonance, making a simple summation unsatisfactory. Shore[34] has derived an equivalent expression that is better suited for a series of closely-spaced resonances because it is mathematically simpler to work with. His expression is

$$
\sigma_t = C + \sum_k \frac{B_k + A_k \epsilon_k}{1 + \epsilon_k^2} \quad , \tag{9}
$$

where C is the background cross section for the series of resonances, the summation is over the k resonances, ϵ_k is as defined in Eq. (4b) for each resonance, and A_k and B_k are the shape parameters for the kth resonance, which we shall refer to as the "Shore parameters". The value C is understood to be a slowly-varying function of the photon energy. As with the Fano parameters, q and ρ^2, the Shore parameters, A and B, are assumed constant in the resonance region.

It is clear that for the case of a single, isolated resonance, the Fano and Shore parametrizations can be expressed in the same mathematical form, as follows:

$$
\sigma_t = \sigma_0 \left[\frac{C_1 + C_2 \epsilon + \epsilon^2}{1 + \epsilon^2} \right] \quad , \tag{10}
$$

where C_1 and C_2 can be expressed in terms of either q and ρ^2 or A and B. We note that although the Shore formalism is to be preferred for multiple resonances, the parameters A and B are not dimensionless

quantities as are q and ρ^2. Because of this, the Fano formalism is more descriptive in the isolated-resonance case.

The formalisms presented so far were derived for the total cross section. In a photoemission experiment, however, partial cross sections are commonly measured. Starace[35] has addressed the problem of several outgoing channels in the vicinity of an autoionization resonance. Davis and Feldkamp[36] and Combet Farnoux[37] have derived equivalent expressions. We shall use the notation of Starace. His expression for the partial cross section of each of the observable photoemission channels, μ, is

$$\sigma(\mu) = \frac{\sigma_0(\mu)}{1 + \epsilon^2} \left[\epsilon^2 + 2\{qRe(\alpha_\mu) - Im(\alpha_\mu)\}\epsilon + 1 \right.$$
$$\left. - 2qIm(\alpha_\mu) - 2Re(\alpha_\mu) + (q^2 + 1)|\alpha_\mu|^2 \right] , \quad (11)$$

where $\sigma_0(\mu)$ is the off-resonance partial cross section for the μth observable final state and ϵ and q are defined in Eqs. (4b) and (5), respectively. The complex parameter, α_μ, is given by[38]

$$\alpha_\mu = \frac{\langle \phi|V|\mu \rangle}{\langle g|\vec{r}|\mu \rangle} \left[\frac{2\pi}{\Gamma} \sum_\mu \langle g|\vec{r}|\mu \rangle\langle \mu|V|\phi \rangle \right] , \quad (12)$$

with Γ given by Eq. (7). The term in brackets is common to all channels. The α_μ parameters can be thought of as replacing ρ^2 as the correlation coefficient for each channel when partial cross sections are measured. It is important to note that each μ represents

an observable photoionization channel [eg. $He^+(1s\epsilon p_{1/2})$]. This restriction was not necessary in the Fano and Shore derivations of the resonance behavior of the total cross section, because the individual photoemission channels only appeared in summations over μ. It is clear that Eq. (11) has the same form as Eq. (10), because it describes the characteristic behavior of a cross section in the vicinity of an autoionization resonance. We will refer to $C_1(\mu)$ and $C_2(\mu)$ as the "Starace parameters".

Because all of the preceding formalisms, whether for total or partial cross sections, have the same mathematical form, it is possible to equate the parameters of the various formalisms, keeping in mind that expression of the parameters in terms of the appropriate matrix elements is only possible if the proper formalism for any given experiment is used. For example, although effective Fano prameters can be derived for the autoionization profile of a partial cross section, it may be misleading to report them as the appropriate resonance parameters, because the expressions given by Fano for q and ρ^2 are not directly applicable to a partial cross section. They can be used in a descriptive context, however. This point will be discussed further in the next subsection.

An additional complication, discussed in Ref. 39, occurs because every peak, m, in a photoemission spectrum contains more than one of the channels, μ, such as the $He^+(1s)$ peak, which has contributions from two outgoing channels; $1s\epsilon p_{1/2}$ and $1s\epsilon p_{3/2}$.[40] Thus, the partial cross section for each photoelectron peak, $\sigma(m)$, is the sum of

severa' $\sigma(\mu)$. The expression for $\sigma(m)$ is of the same form as Eq. (11), but with $\sigma_0(\mu)$ replaced by the off-resonance partial cross section for the unresolved channels, $\sigma_0(m)$, and $\text{Re}(\alpha_\mu)$, $\text{Im}(\alpha_\mu)$, and $|\alpha_\mu|^2$ replaced by $\text{Re}\langle\alpha\rangle_m$, $\text{Im}\langle\alpha\rangle_m$, and $\langle|\alpha|^2\rangle_m$, which are averaged quantities weighted by the $\sigma_0(\mu)$. The Schwartz inequality requires that

$$(\text{Re}\langle\omega\rangle_m)^2 + (\text{Im}\langle\alpha\rangle_m)^2 \leq \langle|\alpha|^2\rangle_m , \tag{13}$$

so that the modified Eq. (11) contains three unknown quantities. Because a fit to the form of Eq. (10) only provides two parameters, it is, in general, impossible to solve for all three unknowns.

The angular-distribution asymmetry parameter, β, can also show effects of autoionization. Kabachnik and Sazhina[41] have shown that for photoionization in the region of an isolated resonance, β is given by

$$\beta = \frac{X'\epsilon^2 + Y'\epsilon + Z'}{A'\epsilon^2 + B'\epsilon + C'} , \tag{14}$$

where A', B' and C' are defined in terms of the parameters for the cross section over the resonance, and X', Y' and Z' are new parameters that depend on the same matrix elements presented earlier, as well as their relative phases. Equation (14) was obtained by the division of two functions of the form of Eq. (10).

The parameters in Eq. (14) have been expressed[41] in terms of the same dipole and Coulomb matrix elements used in the description of

the resonance behavior of total and partial cross sections. The expressions derived by Kabachnik and Sazhina describe the resonance effect upon the asymmetry parameter, β_t, for the <u>total</u> photoelectron flux from a given sample. Except possibly for the special case of no interchannel coupling in the continuum, these expressions cannot describe the resonance behavior of the asymmetry parameter, β_μ, for an individual photoemission channel in terms of these matrix elements. This is especially true for helium because, as we have seen from the discussion in Sect. B, continuum interactions are important. While the form of Eq. (14) correctly describes these "partial β's", no detailed interpretation of the resulting parameters is yet possible.

2. DATA ANALYSIS

In the present experiment, the resonance behavior of the $He^+(n=2)$ partial cross section, branching ratio, and asymmetry parameter in the region below the n=3 threshold was measured. The data for the n=2 satellite are shown in Figs. 6-8. The cross-section data were scaled to the data of Marr and West[1] at the off-resonance energy of 68.9 eV. The remainder of this section is devoted to a discussion of the fitting techniques and assumptions used to describe analytically the cross-section and asymmetry-parameter data in the resonance region.

The $\sigma_{n=2}$ data, shown in Fig. 6, were fitted to the Shore formula, Eq. (9), convoluted with a truncated triangular function of

full-width equal to 0.17 eV (0.43 Å) to account for monochromator
broadening. The off-resonance cross section, C, was taken to be a
linear function of energy. The positions, E_0, and widths, Γ, of the
four resonances were obtained from Woodruff and Samson.[10] The Shore
parameters derived in this way are presented in Table I. Note that
the values for the fourth resonance were held fixed. The solid curve
in Fig. 6 shows this fit, whereas the dashed curve is the same fit,
but with the monochromator broadening removed.

The validity of using the Shore parametrization is dependent upon
the assumption that the resonances are not coupled in any way, or
equivalently, that the series of discrete levels, ϕ_i, do not perturb
each other via Coulomb interactions. Shore[34] has indicated that
this is a good approximation provided that the radiative widths of the
resonance states are small compared to their overall widths. Typical
radiative lifetimes for allowed dipole transitions are in the range
10^{-8}-10^{-9} sec,[42] so the radiative widths are several orders of
magnitude smaller than the resonance widths.

The equivalent Starace parameters for $\sigma_{n=2}$ are also presented
in Table I because they are the most interpretable parameters for a
partial cross section. From the approximation in the previous
paragraph, we know that the Shore parameters derived from the fit to
the $\sigma_{n=2}$ data represent isolated-resonance parameters and can be
equated to the Starace parameters. Use of Eq. (9) in the present
analysis is simply a mathematical construct to derive the appropriate
Starace parameters.

The n=2 satellite branching ratio relative to the 1s main line (Fig. 7) also shows strong resonance effects, mainly due to the changes in $\sigma_{n=2}$. The branching-ratio data were fitted to a ratio of the two cross sections, $\sigma_{n=2}$ and σ_{1s}, each written as in Eq. (9). The parameters for the function in the numerator were taken directly from the fit to $\sigma_{n=2}$. For the denominator, σ_{1s}, the background cross section was taken as a polynomial of first order in energy, and the resonance parameters were varied to get the best fit. The numerator and denominator were convoluted separately with the same monochromator bandpass function used for the fit to the $\sigma_{n=2}$ data. The parameters for σ_{1s} for the 3s3p resonance from this fit can be found in Table II. The uncertainties in the σ_{1s} parameters for the higher-lying resonances derived from the branching-ratio fit are too large for these parameters to be reported with any confidence.

The asymmetry parameter for the n=2 satellite is strongly affected by autoionization, because the peak includes contributions from two satellites with very different off-resonance asymmetry parameters. Our results are shown in Fig. 8. We also have measured β_{1s} in the resonance region and found it to be 2.00(5). The $\beta_{n=2}$ data were fitted in a manner identical to the fit to the branching-ratio data, except the parameters in the denominator were taken from the fit to $\sigma_{n=2}$ (Table I). The function used was

$$\beta_{n=2} = \frac{\sum\limits_{k} \dfrac{Y_k + X_k \epsilon_k}{1 + \epsilon_k^2} + Z}{\sum\limits_{k} \dfrac{B_k + A_k \epsilon_k}{1 + \epsilon_k^2} + C} \quad . \tag{15}$$

The background value, Z, was assumed to be a second–order polynomial in energy. The resonance parameters, X_k and Y_k, are presented in Table III, where they have been used to determine X_k', Y_k' and Z_k' as in Eq. (14). As with the n=2 partial cross–section fit, we have equated the parameters in the fit to the numerator of $\beta_{n=2}$ with the corresponding single–resonance parameters described by Kabachnik and Sazhina.[41] The parameters A_k', B_k' and C_k' are not shown, but can easily be derived from the values in Table I and Eqs. (14) and (15). We present these "Kabachnik–Sazhina parameters" for $\beta_{n=2}$, with the caveat that the definitions given in Ref. 41 do not allow easy interpretation for an individual photoemission line.

The fit to the $\beta_{n=2}$ data, including monochromator broadening, is shown in Fig. 8. The problem of deconvolution of instrumental broadening from the measured asymmetry parameters is not straightforward, especially when the monochromator bandpass is on the order of, or larger than, the resonance linewidth. The method used here is the same as that described for the fit to R_{21}, but using Eq. (15). This method was chosen because the form of Eq. (15) is more amenable to fitting a series of closely–spaced resonances, and because the measured asymmetry parameters are derived from the ratio of peak intensities in two analyzers. The deconvoluted curve is shown in Fig. 8.

3. RESULTS - CROSS SECTIONS AND BRANCHING RATIOS

The parameters for $\sigma_{n=2}$ for the first four members of the Rydberg series leading to the n=3 threshold are listed in Table I, along with the results of Woodruff and Samson,[10] which agree with our results except for the 3s3p resonance. We attribute this small difference to the fact that the fit by Woodruff and Samson does not agree with their data for the first resonance as well as the fit presented here. The parameters for each member of the Rydberg series are fairly similar, as originally predicted by Fano and Cooper.[21] Results of several calculations[22,32,43-48] of these positions and widths are summarized in Ref. 10. Differences in the background cross sections (C and σ_0 in Table I) are due to differences in the scaling of the present data and the data in Ref. 10.

From the satellite branching ratio in Fig. 7, we have determined rough values of the σ_{1s} resonance parameters. Qualitatively, we find that σ_{1s} has the same phase as $\sigma_{n=2}$ for the 3s3p resonance. Our qualitative, as well as quantitative (Table II), results are in complete agreement with recently published data on σ_{1s}.[12] Similarly, because σ_t is just the sum of σ_{1s} and $\sigma_{n=2}$, the total cross section also must have the same phase for this resonance. Quantitatively, the situation for σ_t is summarized in Table IV. This qualitative interpretation is in conflict with the phase of σ_{1s} over the 3s3p resonance that is required by the shape of σ_t measured by Dhez and Ederer[20] combined with the shape of $\sigma_{n=2}$ from the

present results (the latter being in agreement with the fluorescence measurements of Woodruff and Samson[10] over the same region). The results from Dhez and Ederer would require σ_{1s} and $\sigma_{n=2}$ to have opposite phases for this resonance because the effect on σ_t measured by them is small enough that when the two partial cross sections are added to get the total cross section, their effects would have to cancel. This requires that σ_{1s} reach a maximum below the resonance energy and a minimum above that energy. This conclusion was first reached by Woodruff and Samson,[10] but is inconsistent with our results, as well as the direct measurement of σ_{1s}.[12] Because this cancellation does not occur, the strength of the effect on σ_t (as measured by ρ^2) must be significantly larger than that reported by Dhez and Ederer. This discrepancy may be explained by reference to Table I in Ref. 20. This table lists the Shore parameters for a series of five transmission scans taken at three different pressures; 50, 90 and 120 torr. Calculating q and ρ^2 for each scan shows a definite pressure dependence of ρ^2 (0.009 at 120 torr, 0.013 at 90 torr, and 0.018 at 50 torr). Exactly what can cause such a pressure effect on ρ^2 is unclear.

Our value of q also disagrees with the previous result. While this may be due to our experimental uncertainties, it also could be the result of the normalization procedure used in the earlier work. By normalizing the data at 177.22Å, which is an energy near the center of the resonance, that point is forced to lie on the background curve, fixing the shape of the resonance with respect to the background cross

section and thus affecting q.

The present results are also to be compared with previous estimates of the resonance parameters. Fano and Cooper[21] estimated q and ρ^2 to be 1.7 and 0.01, respectively. Calculations by Senashenko and Wague[22] using the diagonalization approximation yielded q = 1.31 and ρ^2 = 0.019. Both of these calculations disagree with the larger value of ρ^2 inferred here. For the first estimate, however, it may be possible to trace one reason for this disagreement. In estimating q, Fano and Cooper assumed that the matrix elements involving the 1sεp continuum state for the 3s3p resonance are not significantly different than similar matrix elements for the 2s2p resonance. This assumption seems to imply, at least, that σ_{1s} has the same phase for both the 2s2p and the 3s3p resonances. However, σ_{1s} has opposite phases for these two resonances. The effect on the resulting values of q and ρ^2 for the total cross section is not clear. One other calculation[43] of σ_t for the 3s3p resonance has also been performed that reproduces the correct qualitative shape of the resonance, but no parameters were extracted because of the small number of points evaluated.

The remainder of this subsection will illustrate some of the quantitative results that can be derived from the measured parameters (Table I) and the parameters inferred for σ_{1s} and σ_t (Tables II and IV). We wish to stress that caution should be exercised concerning the actual values presented below, but the procedures described are useful in general for autoionization phenomena.

The oscillator strength, f, for the 3s3p resonance can be obtained from the Fano parameters for the total cross section. It is given by[49]

$$f = (0.195 \text{ Ry}^{-1}\text{Mb}^{-1}) \ q^2{}_\rho{}^2 \ \sigma_t \ \Gamma \ , \tag{16}$$

with Γ expressed in Rydbergs and σ_t expressed in Mb. Using the values in Table IV, we find $f = 2.0 \times 10^{-4}$, which agrees well with the previous estimate[21] of 1.2×10^{-4}. A similar, but possibly more descriptive, expression for f is obtained[50] by replacing q^2 in Eq. (16) with $(q^2 - 1)$. The result for this case is -8.1×10^{-5}, indicating that σ_t in the vicinity of the 3s3p resonance exhibits a net loss in oscillator strength compared to the background cross section. The latter value of f is more descriptive of autoionization in the sense that it is a measure of the spectral repulsion part of the autoionization profile.

Useful information also may be derived from the partial cross sectons. Although, as we have pointed out, it is generally impossible to determine all three unknowns in Eq. (13), the simplicity of the helium system allows us to do so in a manner similar to the method described in an earlier paper.[39] The following discussion is limited to the 3s3p resonance, but similar results are expected for the higher-lying resonances. For $He^+(1s)$ production, there are only two out-going channels, μ: $1s\epsilon p_{1/2}$ and $1s\epsilon p_{3/2}$.[40] The dipole and Coulomb matrix elements for these two channels help determine two of the α_μ parameters: $\alpha_{1s\epsilon p_{1/2}}$ and $\alpha_{1s\epsilon p_{3/2}}$. Of course, both of these channels

are present in the He^+(1s) peak (m=1s). In this case, however, because the spin-orbit interaction in the ϵp continuum is small, and because β_{1s} is identically 2.0 over the resonance, the Schwartz inequality, Eq. (13), becomes an equality. Equations (10), (11) and (13) and the Starace parameters in Table II may then be used to obtain $Re\langle\alpha\rangle_{1s}$, $Im\langle\alpha\rangle_{1s}$ and $\langle|\alpha|^2\rangle_{1s}$. The solution involves a complicated quadratic equation for $Re\langle\alpha\rangle_{1s}$. The solution with $\langle|\alpha|^2\rangle_{1s} > 2$ is dismissed, because it would require that the total cross section have $\rho^2 > 1$. The parameters for the correct solution are given in Table V. It is also possible to determine the non-averaged quantities, $Re(\alpha_{1s\epsilon p_j})$, $Im(\alpha_{1s\epsilon p_j})$ and $|\alpha_{1s\epsilon p_j}|^2$, where j can have the values 1/2 or 3/2, because our earlier assumption that Eq. (13) is an equality means that the matrix elements for the two outgoing channels in the 1s peak are identical for the dipole and Coulomb interactions. The averaged quantities for the 1sϵp final state in Table V are then just averages of identical quantities.

From Eqs. (15) and (16) in Ref. 39, we can determine the partial linewidths, Γ_{1s} and $\Gamma_{n=2}$, for the two final states. Both of these partial widths are included in Table V. The large difference in the partial widths illustrates why the effect of the resonance on σ_{1s} is small relative to the effect on $\sigma_{n=2}$, even though σ_0(1s) is an order of magnitude larger than σ_0(n=2). The partial widths can be interpreted as an additional measure ($\langle|\alpha|^2\rangle_m$ is the other one) of the strength of the resonance effect on an individual final state. As we did with the α parameters for the 1s level, we can break down the

contributions to Γ_{1s} into partial widths for each outgoing channel, being careful to account for the multiplicities of the two outgoing channels. The results are $\Gamma_{1s\epsilon p_{1/2}}/\Gamma = 0.004$ and $\Gamma_{1s\epsilon p_{3/2}}/\Gamma = 0.009$. The partial widths (in percent) derived here agree very well with previous calculations.[22,32]

Because we have already found $\langle |\alpha|^2 \rangle_{1s}$, we can use Eq. (16) in Ref. 38 to find $\langle |\dot{\alpha}|^2 \rangle_{n=2}$. Having done this, $C_1(n=2)$ and $C_2(n=2)$ for the 3s3p resonance from Table I can be used with Eqs. (10) and (11) to find $\mathrm{Re}\langle \alpha \rangle_{n=2}$ and $\mathrm{Im}\langle \alpha \rangle_{n=2}$. These values are also presented in Table V. We note that for the α-parameters for $\sigma_{n=2}$, Eq. (13) appears to be a true inequality. Because the satellite peak containing the 2s and 2p final states includes seven possible outgoing channels, no further information can be obtained.

A check of the α_μ parameters can be made as described in Ref. 39. The results in Table V satisfy this check to well within the statistical errors, suggesting that no major systematic errors are present in the data analysis.

Some interpretation of the α_μ parameters can be made, keeping in mind that the actual values may not be very accurate. The positive values of $\mathrm{Re}\langle \alpha \rangle_m$ for both the 1s and n=2 levels indicate that these two resonance profiles should have the same phase over the resonance, as we have suggested. The approximately zero values for $\mathrm{Im}\langle \alpha \rangle_{1s}$ and $\mathrm{Im}\langle \alpha \rangle_{n=2}$ show that the α_μ parameters are essentially real numbers. This result seems fortuitous, because it probably does not imply, as discussed by Combet Farnoux,[37] that interchannel coupling in the

continuum is weak. In fact, because the n≈2 peak is a satellite of the 1s peak, interchannel coupling in this case is important (see Sect. B). It might prove interesting to measure the α parameters for the individual final states, 2s and 2p. The strong coupling between 2sϵp and 2pϵs may result in α parameters that are complex. A detailed flourescence experiment, similar to that done by Woodruff and Samson,[10] could measure these parameters.

To this point, we have only derived parameters which depend on several of the dipole and Coulomb matrix elements. It is possible, however, for the case of the 3s3p resonance, to determine directly the squares of three of the matrix elements, including all of those describing autoionization into the 1sϵp continuum. The Coulomb matrix elements $|\langle 3s3p|V|1s\epsilon p_j\rangle|^2$, with j=1/2 or 3/2, can be obtained from Eq. (7) for the partial decay width, $\Gamma_{1s} = 0.0023$ eV, by properly accounting for the multiplicity of the 1sϵp$_j$ states. The dipole matrix elements for continuum absorption, $|\langle 1s\epsilon p_j|\vec{r}|1s^2\rangle|^2$, can be determined from σ_{1s} as described in Ref. 21 and again considering the multiplicities. The dipole matrix elements can also be expressed as oscillator strengths. The dipole matrix element for the discrete transition $1s^2 \rightarrow 3s3p$ can be determined[21] from the oscillator strength, f, derived above. All of these results are listed in Table VI, along with estimates of two of the matrix elements by Fano and Cooper.[21] Their results agree with ours to within a factor of 2. One additional parameter can also be derived. The square of the term in brackets in Eq. (13) can be determined by using $\langle|\alpha|^2\rangle_{1s}$ from

Table V and the matrix elements in Table VI. We find this term to have the value 36 Mb/Ry^2.

A review of the results of this subsection is useful. Quantitatively, we have presented parameters defining the resonance profiles of $\sigma_{n=2}$ and R_{21}. From these results, we have inferred the qualitative behavior of σ_{1s} and σ_t for the 3s3p resonance only, concluding that the phases for $\sigma_{n=2}$, σ_{1s}, and σ_t are the same for this resonance. This result agrees with recent photoemission data, but disagrees with an earlier photoabsorption measurement. Exercising caution for the quantitative results, we have determined parameters that quantify the qualitative behavior of σ_{1s} and σ_t, in order to illustrate methods for extracting information from measurements of autoionization phenomena. The results, such as α parameters and dipole matrix elements, which are obtained in this way can be useful in describing the aspects of interchannel coupling in the continuum[37] and for comparison with theoretical calculations of resonance behavior. Values for individual matrix elements may prove particularly helpful as a guide to determining appropriate wavefunctions and other parameters for calculations. As a final point, we again wish to stress that while the results of this experiment are not sufficiently accurate to provide a complete and quantitative interpretation, we have attempted to document fully one of the first measurements of this kind.

4. RESULTS - ASYMMETRY PARAMETERS

The data in Fig. 8 mark the first detailed measurement of a satellite asymmetry parameter over autoionization resonances. The accompanying parameters in Table III vary only slightly over the members of the Rydberg series, as first predicted by Dill.[51]

Because the angular distributions of all of the helium photo-emission peaks (there are only 2) were measured in this experiment, it is possible to determine β_t from

$$\beta_t = \frac{\beta_{1s} + R_{21}\beta_{n=2}}{1 + R_{21}} , \tag{17}$$

with $\beta_{1s} = 2$, and R_{21}, $\sigma_{n=2}$ and $\beta_{n=2}$ given by Eqs. (10) and (15) for the 3s3p resonance only. The resulting β_t has the same mathematical form as $\beta_{n=2}$, and the Kabachnik-Sazhina parameters describing it are given in Table VII. The off-resonance value of β_t is approximately 1.8, with deviations due to autoionization of only ~0.1, as expected because the dominant 1s channel shows no effect in β_{1s}. It is hoped that these results, as well as those for $\beta_{n=2}$, will spur further theoretical development regarding the detailed behavior of angular distributions of individual photoemission lines in the vicinity of autoionization resonances. Complete understanding of this phenomenon awaits further theoretical and experimental work.

In Sect. B we were able to derive the ratio $R = \sigma_{2p}/\sigma_{2s}$ from the measured off-resonance $\beta_{n=2}$ data and calculated values of β_{2p}.

We are unable to do this in the resonance region because the resonance behavior of β_{2p} is unknown, but certain qualitative statements can be made concerning the effects on R of the 3s3p resonance. For the following discussion, the reader is referred to the deconvoluted curves in Figs. 6 and 8.

Figure 6 shows that the $n=2$ partial cross section drops nearly to zero at the minimum of the 3s3p resonance. From Fig. 5, the background value of R at 70 eV is ~2.2. To account for the minimum in $\sigma_{n=2}$, both σ_{2p} and σ_{2s} must be going through a minimum at the energy of the minimum in $\sigma_{n=2}$. Furthermore, both of these minima occur on the low-energy side of the 3s3p resonance. In other words, we can conclude that both σ_{2p} and σ_{2s} are affected by the resonance and that they have the same phase. The question then arises of whether or not these effects manifest themselves in an effect on R. If R is left un-affected, then the measured change in $\beta_{n=2}$ [see Eq. (2)] must be due solely to changes in β_{2p} (assuming that β_{2s} is always 2.0, just like β_{1s}). However, examination of the minimum in $\beta_{n=2}$ on the high-energy side of the resonance shows that even if β_{2p} is -1 at this energy, a value of R = 2.2 is not large enough to yield [see Eq. (3)] the deconvoluted value of $\beta_{n=2} = -0.25$ from Fig. 8. The values of R = 2.2 and $\beta_{2p} = -1$ yield $\beta_{n=2} = -0.06$. The uncertainty in the minimum of the deconvoluted curve for $\beta_{n=2}$ is ~0.1. Therefore, our value of $\beta_{n=2} = -0.25$ suggests that R shows a positive deviation from its background value of 2.2 on the high-energy side of the 3s3p resonance. Because R must have the same shape as the satellite

branching—ratio over an autoionization resonance, it must reach a minimum on the low—energy side of the 3s3p resonance as well. No limits can be placed on the value of this minimum. The conclusion then, is that R drops to a minimum on the low—energy side and rises to a maximum on the high—energy side of the 3s3p resonance. This behavior is most likely caused by σ_{2p} and σ_{2s} having similar profiles, but with σ_{2p} reaching its minimum at a slightly lower energy than σ_{2s}. This implies that the Starace parameters, $C_1(2p)$ and $C_2(2p)$, are slightly larger than $C_1(2s)$ and $C_2(2s)$, respectively. We expect the higher members of this series to have similar effects on R, because partial cross sections tend to retain the same shape over a Rydberg series.[21]

D. CONCLUSIONS

The photoionization of helium to the n=2 excited state of the helium ion has provided several interesting results. The off—resonance measurements of $\beta_{n=2}$ have shown additional clear evidence that the n=2 satellite is mainly comprised of the 2p final state near threshold. Furthermore, the strong energy dependence of R has given some insight into the understanding of electron correlation in atomic systems: the helium case being especially useful because of its relative simplicity.

For the He^+(n=2) satellite, the partial cross—section, branching—ratio, and asymmetry—parameter behavior has been measured over the major Rydberg series leading to the n=3 threshold. These

angular-distribution measurements are the first of their kind for a satellite line. Parameters describing all of these resonance effects have been presented. From the angular-distribution results, the qualitative behavior of R over the resonances has been inferred.

The qualitative behavior of the total and 1s cross sections has been determined for the 3s3p resonance. The results have mixed agreement with previous measurements, and more work at higher resolution on the total cross section of helium above the $n \geq 2$ thresholds is recommended to verify our conclusions. The 1s cross-section results have been used in an illustrative way to indicate how information about autoionization behavior in photoemission can be extracted.

where L_t is the length of the flight path of the TOF analyzers (~29 cm), and C is a constant. This method works at SSRL because the synchrotron radiation is pulsed as a result of the bunched structure of the electrons in the storage ring. The pulses are narrow (~0.3 nsec) and spaced far enough apart in time (195-780 nsec depending on the running mode of SPEAR) to allow electrons of most energies to be collected between consecutive pulses with moderate-to-good time resolution. The limitation on the TOF analyzer resolution at low electron kinetic energies is the uncertainty in the flight path (and hence the flight time) because of the finite width (3 mm) of the photon beam at the interaction region. For the grasshopper mono-chromator, the resolution was typically 2.5% of the kinetic energy of the electrons for the $0°$ analyzer, and 3.5-4.0% for the $54.7°$ detector. At high kinetic energies (>100-200 eV), other contributions to the resolution become important, and the poor overall analyzer resolution is prohibitive to doing well-resolved experiments.

The TOF method is well-suited to gas-phase photoelectron spectroscopy because it collects nearly all energies of photoelectrons simultaneously, providing an excellent signal-to-noise ratio for many experiments. Simultaneous measurement of photoelectron peak intensities at two angles yields asymmetry parameters (see Eq. 4, Chapter I) that are independent of variations in the photon flux and gas pressure. Peak intensities at $54.7°$ (the 'magic angle'), for which $P_2(\cos\theta)$ vanishes, are directly proportional to photoion-ization cross sections after normalization to photon flux and gas

15. V.L. Jacobs and P.G. Burke, J. Phys. B $\underline{5}$, L67 (1972).

16. T.N. Chang, J. Phys. B $\underline{13}$, L551 (1980).

17. J.A. Richards, Honours Thesis, Monash University (1981).

18. K.A. Berrington, P.G. Burke, W.C. Fon, and K.T. Taylor, J. Phys. B $\underline{15}$, L603 (1982).

19. J.A. Richards and F.P. Larkins, J. Electron Spectrosc. $\underline{32}$, 193 (1983).

20. P. Dhez and D.L. Ederer, J. Phys. B $\underline{6}$, L59 (1973).

21. U. Fano and J.W. Cooper, Phys. Rev. $\underline{137}$, A1364 (1965).

22. V.S. Senashenko and A. Wagué, J. Phys. B $\underline{12}$, L269 (1979).

23. S.T. Manson, J. Electron Spectrosc. $\underline{9}$, 21 (1976).

24. J.A. Richards and F.P. Larkins (private communication).

25. T. Ishihara, J. Mizuno, and T. Watanabe, Phys. Rev. A, $\underline{22}$, 1552 (1980).

26. H.P. Kelly, Phys. Rev. A $\underline{6}$, 1048 (1972).

27. R.L. Brown, Phys. Rev. A $\underline{1}$, 341 (1970).

28. J.M. Bizau, F.J. Wuilleumier, D.L. Ederer, P. Dhez, S. Krummacher, and V. Schmidt (unpublished).

29. C.H. Greene, Phys. Rev. Lett. $\underline{44}$, 869 (1980).

30. C.H. Greene (private communication).

31. R.P. Madden and K. Codling, Astrophys. J. $\underline{141}$, 364 (1965).

32. D.R. Herrick and O. Sinanoğlu, Phys. Rev. A $\underline{11}$, 97 (1975).

33. U. Fano, Phys. Rev. $\underline{124}$, 1866 (1961).

34. B.W. Shore, Phys. Rev. $\underline{171}$, 43 (1968).

35. A.F. Starace, Phys. Rev. A $\underline{16}$, 231 (1977).

36. L.C. Davis and L.A. Feldkamp, Phys. Rev. B 15, 2961 (1977); 23, 6239 (1981).

37. F. Combet Farnoux, Phys. Rev. A 25, 287 (1982).

38. P.C. Kemeny, J.A.R. Samson, and A.F. Starace, J. Phys. B 10, L201 (1977).

39. P.H. Kobrin, U. Becker, S. Southworth, C.M. Truesdale, D.W. Lindle, and D.A. Shirley, Phys. Rev. A 26, 842 (1982).

40. Although the $1s\epsilon p_{1/2}$ and $1s\epsilon p_{3/2}$ final states are not resolved in this work, they have to be considered here for the later discussion because of their different multiplicities. Ignoring this point can lead to incorrect interpretation of the data.

41. N.M. Kabachnik and I.P. Sazhina, J. Phys. B 9, 1681 (1976).

42. G. Herzberg, Molecular Spectra and Molecular Structure I. Spectra of Diatomic Molecules (Van Nostrand, New York, 1950).

43. S. Ormonde, W. Whitaker, and L. Lipsky, Phys. Rev. Lett. 19, 1161 (1967).

44. P.G. Burke and A.J. Taylor, J. Phys. B 2, 44 (1969).

45. R.S. Oberoi, J. Phys. B 5, 1120 (1972).

46. K.T. Chung and I. Chen, Phys. Rev. Lett. 28, 783 (1972).

47. Y.K. Ho, J. Phys. B 12, 387 (1979).

48. Y.K. Ho, J. Phys. B 15, L691 (1982).

49. U. Fano and J.W. Cooper, Rev. Mod. Phys. 40, 441 (1968).

50. P.G. Burke and D.D. McVicar, Proc. Phys. Soc. (London) 86, 989 (1965).

51. D. Dill, Phys. Rev. A 7, 1976 (1973).

Table I. Parameters for the He^+(n=2) partial cross section for the first 4 members of the 1_n Rydberg series. The background cross section, σ_0 (Mb), was taken to be $0.216 - 0.0017(E)$, where E is the photon energy in eV. Numbers in parentheses represent statistical errors only.

Resonance		Shore parameters(Mb)			Starace parameters	
		This work	WS[a]		This work	WS[a]
1_3	A	0.120(2)	0.081(14)	c_1	0.55(2)	0.24(11)
E_0=69.917 eV[a]	B	-0.044(2)	-0.065(8)	c_2	1.24(2)	0.94(18)
Γ=0.178 eV[a]	C	0.097(1)	0.086(7)	σ_0(Mb)	0.097(1)	0.086(7)
1_4	A	0.086(5)	0.079(17)	c_1	0.35(5)	0.23(13)
E_0=71.601 eV[a]	B	-0.061(5)	-0.066(10)	c_2	0.92(5)	0.92(21)
Γ=0.096 eV[a]	C	0.094(1)	0.086(7)	σ_0(Mb)	0.094(1)	0.086(7)
1_5	A	0.080(7)	0.088(21)	c_1	0.45(8)	0.49(15)
E_0=72.181 eV[a]	B	-0.051(7)	-0.044(12)	c_2	0.86(8)	1.02(26)
Γ=0.067 eV[a]	C	0.093(1)	0.086(7)	σ_0(Mb)	0.093(1)	0.086(7)
1_6	A	0.080(fix)	0.085(28)	c_1	0.45(fix)	0.23(20)
E_0=72.453 eV[a]	B	-0.051(fix)	-0.066(16)	c_2	0.86(fix)	0.99(34)
Γ=0.038 eV[a]	C	0.093(1)	0.086(7)	σ_0(Mb)	0.093(1)	0.086(7)

[a]Woodruff and Samson, Ref. 10.

Table II. Parameters for the He^+(1s) partial cross section for the 3s3p resonance. The background cross section, σ_0 (Mb), was taken to be $2.87 - 0.0283(E)$, where E is the photon energy in eV. Numbers in parentheses represent statistical errors only.

Effective Fano parameters[a]	Starace parameters[a]
$q = 1.1(3)$	$C_1 = 1.01(3)$
$\rho^2 = 0.046(30)$	$C_2 = 0.10(7)$
$\sigma_0 = 0.892(20)$ Mb	$\sigma_0 = 0.892(20)$ Mb

[a]$E_0 = 69.917(12)$ eV and $\Gamma = 0.178(12)$ eV from Ref. 10.

Table III. Parameters for $\beta_{n=2}$ for the first 4 members of the 1_n Rydberg series. The background value, Z (Mb), was taken to be $2.28 + 0.0103(E) - 0.00061(E^2)$, where E is the photon energy in eV. Numbers in parentheses represent statistical errors only.

n	Fit parameters(Mb)			KS parameters(Mb)[a]		
	X	Y	Z	X'	Y'	Z'
3	-0.030(6)	-0.037(5)	0.021(1)	0.021(1)	-0.030(6)	-0.016(5)
4	-0.031(9)	-0.037(9)	0.036(2)	0.036(2)	-0.031(9)	-0.001(9)
5	-0.031(14)	-0.040(14)	0.041(3)	0.041(3)	-0.031(14)	0.001(14)
6	-0.031(fix)	-0.040(fix)	0.043(3)	0.043(3)	-0.031(fix)	0.003(fix)

[a]Kabachnik and Sazhina, Ref. 41.

Table IV. Parameters for the total cross section of helium for the 3s3p resonance, derived from the results in Tables I and II. The numbers in parentheses represent statistical errors only.

	Fano parameters			Shore parameters(Mb)	
	This work	DE[a]		This work	DE[a]
q	0.84(30)	1.36(20)	A	0.18(8)	0.032(6)
ρ^2	0.11(3)	0.012(3)	B	−0.032(56)	0.010(5)
σ_0(Mb)	0.989(20)	0.957(30)	C	0.989(20)	0.957(30)
Γ(eV)	0.178(12)[b]	0.132(14)			
E_0(eV)	69.917(12)[b]	69.919(7)			

[a]Dhez and Ederer, Ref. 20.

[b]From Ref. 10.

Table V. α-parameters and partial linewidths for the 3s3p resonance.

Final state	$\mathrm{Re}\langle\alpha\rangle_m$	$\mathrm{Im}\langle\alpha\rangle_m$	$\langle|\alpha|^2\rangle_m$	$(\Gamma_m/\Gamma)\times100$
$1s\epsilon p$	0.023(21)	−0.03(4)	$0.0016\ ^{+0.0020}_{-0.0016}$	$1.3\ ^{+1.7}_{-1.3}$
$\left.\begin{array}{c}2s\epsilon p\\ 2p\epsilon s\end{array}\right\}\,n{=}2$	0.99(15)	0.2(3)	1.1(3)	$98.7\ ^{+1.3}_{-1.7}$

Table VI. Matrix elements for the 3s3p resonance.

| Matrix element | Amplitude | |
	This work	Fano and Cooper[21]
$\vert \langle 3s3p \vert \vec{r} \vert 1s^2 \rangle \vert^2$	1.1×10^{-3} Mb	6.8×10^{-4} Mb
$\vert \langle 1s\epsilon p_j \vert \vec{r} \vert 1s^2 \rangle \vert^{2a,b}$	0.10 Mb/Ry	
$\vert \langle 3s3p \vert V \vert 1s\epsilon p_j \rangle \vert^{2b}$	4.5×10^{-6} Ry	4.7×10^{-6} Ry[c]

[a]The corresponding oscillator strength, df/dE, is 0.0014 eV^{-1}.

[b]$j = 1/2, 3/2$.

[c]The value given by Fano and Cooper is for the sum over all the channels contributing to the 1s peak. We have divided their value by 6 for comparison.

Table VII. Kabachnik-Sazhina parameters for the angular distribution
of the total photoelectron flux from helium for the 3s3p resonance.
The numbers in parentheses represent statistical errors only.

$X' = 1.81(4)$	$A' = 0.99(2)$
$Y' = 0.15(13)$	$B' = 0.18(8)$
$Z' = 1.79(7)$	$C' = 0.96(6)$

Fig. 1. Energy-level diagram for helium. DI = direct ionization. AI = autoionization. The energy scale above the break is expanded four times relative to the energy scale below the break.

Fig. 2. TOF photoelectron spectrum of helium taken with the 54.7° detector at a photon energy of 80 eV. The peak labels indicate the principal quantum number of the single-electron final state of the ion.

Fig. 3. Branching ratio, $R_{21} = \sigma_{n=2}/\sigma_{1s}$, for the $He^+(n=2)$ satellite relative to the 1s main line. Experimental results; solid circles - present results; solid square - Samson, Ref. 4; open circle - Krause and Wuilleumier, Ref. 6; X - Wuilleumier et al., Ref. 8. Theoretical curves; long-short dashed - Salpeter and Zaidi, Ref. 13; dashed-dotted - Jacobs, Ref. 14; solid - Jacobs and Burke, Ref. 15; long-dashed - Chang, Ref. 16; short-dashed - Richards, Ref. 17. Where applicable (Refs. 14-17), we have plotted only the velocity results for consistency.

Fig. 4. Asymmetry parameter of the $He^+(n=2)$ satellite as a function of photon energy. Experimental results; solid circles - present results; open circles - Bizau et al., Ref. 9; X - Schmidt et al., Ref. 11; open squares - Morin et al., Ref. 12. Some error bars have been omitted for clarity. Theoretical curves; solid - Jacobs and Burke, Ref. 15; dashed - Chang from Bizau et al., Ref. 9. Also shown are calculations

of the asymmetry parameter for the 2p final state by Jacobs
and Burke (Ref. 15) and Chang (Ref. 9). The velocity forms of
the calculations have been plotted in all cases.

Fig. 5. The subshell branching ratio, $R = \sigma_{2p}/\sigma_{2s}$, for the He^+(n=2)
satellite as a function of photon energy. Experimental
results; solid circles — present results; solid squares —
Woodruff and Samson, Ref. 10; open circles — Bizau et al., Ref.
9; X — Schmidt et al., Ref. 11; open squares — Morin et al.,
Ref. 12. Some error bars have been omitted for clarity.
Theoretical curves; dashed-dotted — Jacobs, Ref. 14; solid —
Jacobs and Burke, Ref. 15; long-dashed — Chang, Ref. 16;
short-dashed — Richards and Larkins, Ref. 19; long-short
dashed — Berrington et al., Ref. 18. From Berrington et al.
we show the length form of their calculation, which the
authors predict to be more accurate than the velocity form.
The remainder of the curves are velocity forms.

Fig. 6. Partial cross section of the He^+(n=2) satellite in the res-
onance region below the n=3 threshold, scaled to Marr and West
(Ref. 1) at 68.9 eV. The solid curve is a fit to the data
using the form of Eq. (9). The dashed curve is the same fit
with the monochromator broadening of 0.17 eV (0.43 Å) removed.

Fig. 7. Branching ratio, $R_{21} = \sigma_{n=2}/\sigma_{1s}$, for the He^+(n=2)
satellite relative to the 1s main line in the resonance region
below the n=3 threshold. The solid and dashed curves are fits
to the data with and without monochromator broadening,

respectively, as described in the text.

Fig. 8. Asymmetry parameter of the $He^+(n=2)$ satellite in the resonance region below the $n=3$ threshold. The solid curve is a fit to the data using the form of Eq. (15). The dashed curve is the same fit with the monochromator broadening removed by the method described in the text.
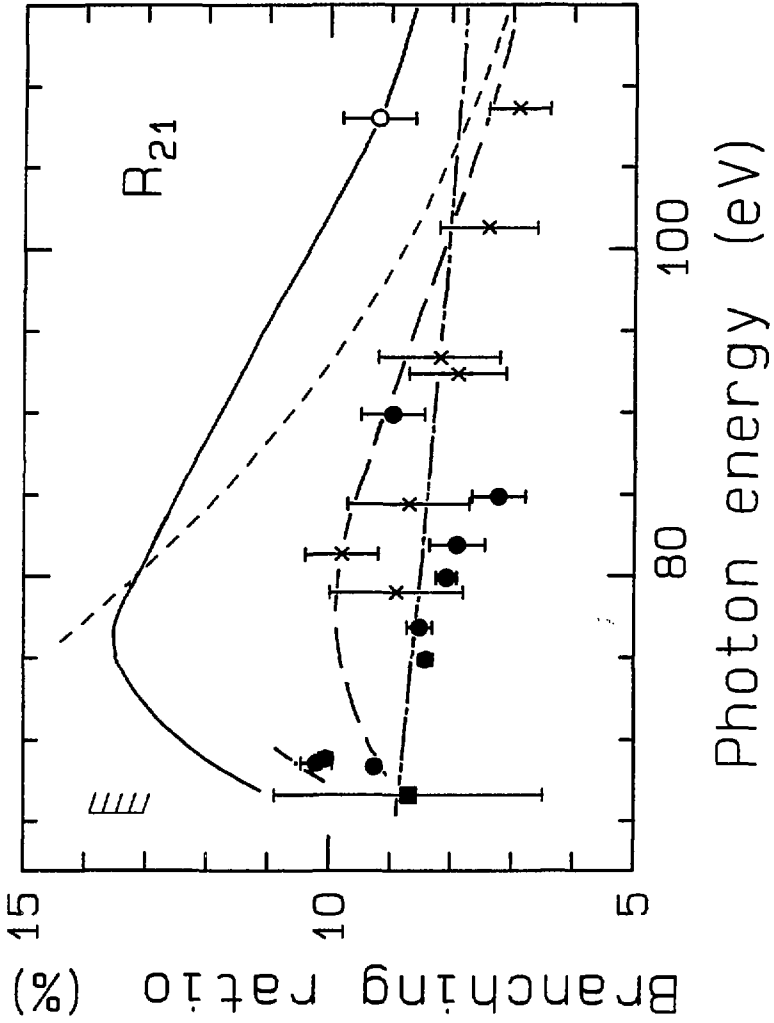
Figure 1

XBL 834-9460
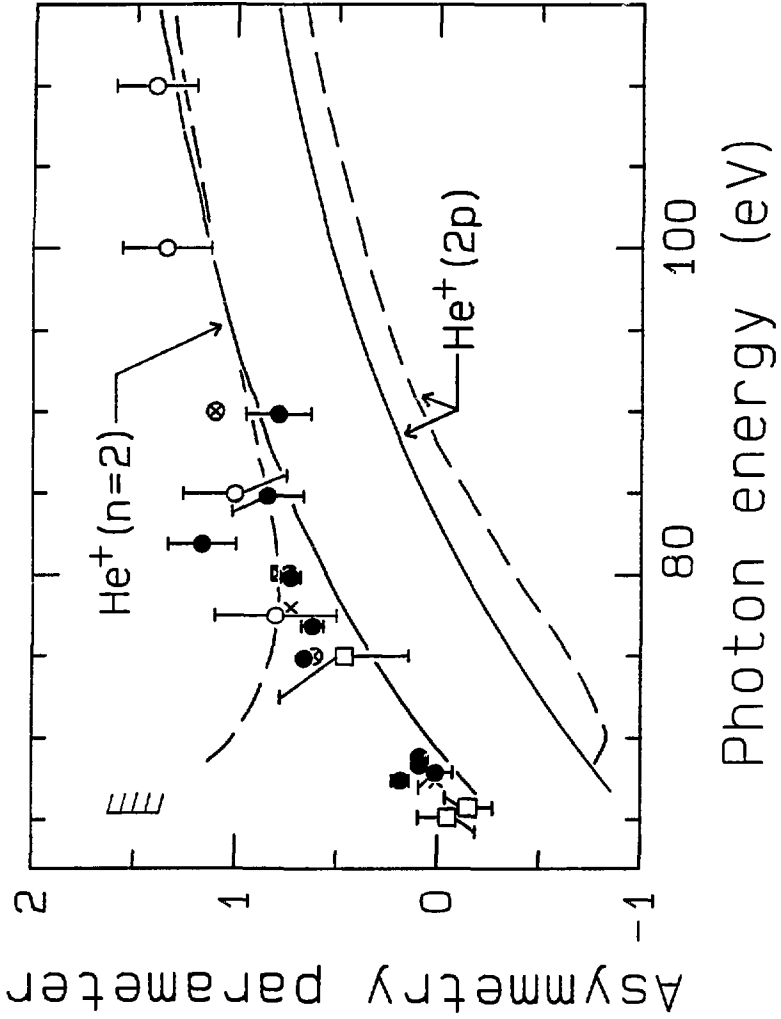
XBL 834-9461

Figure 2

R$_{21}$

Photon energy (eV)

Branching ratio (%)
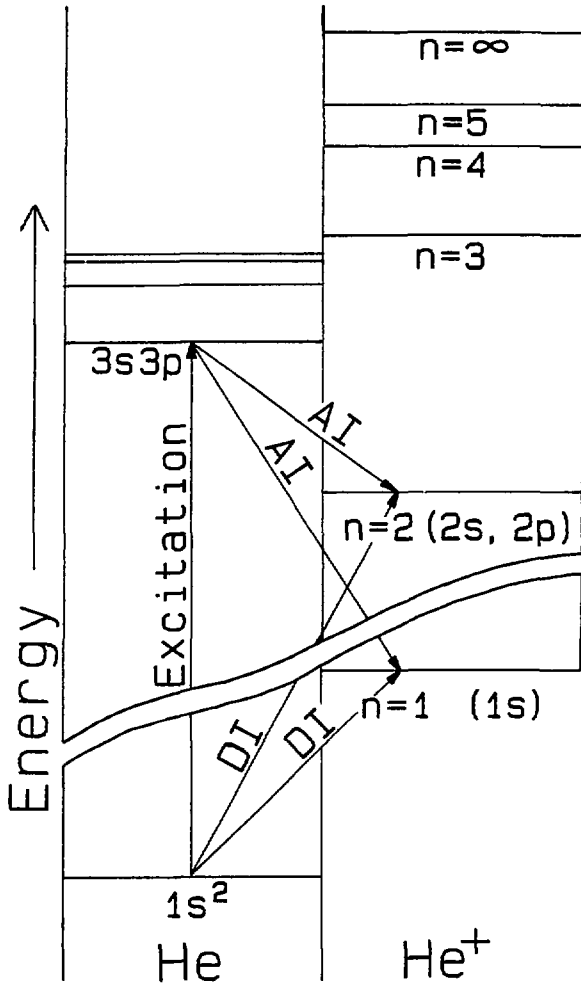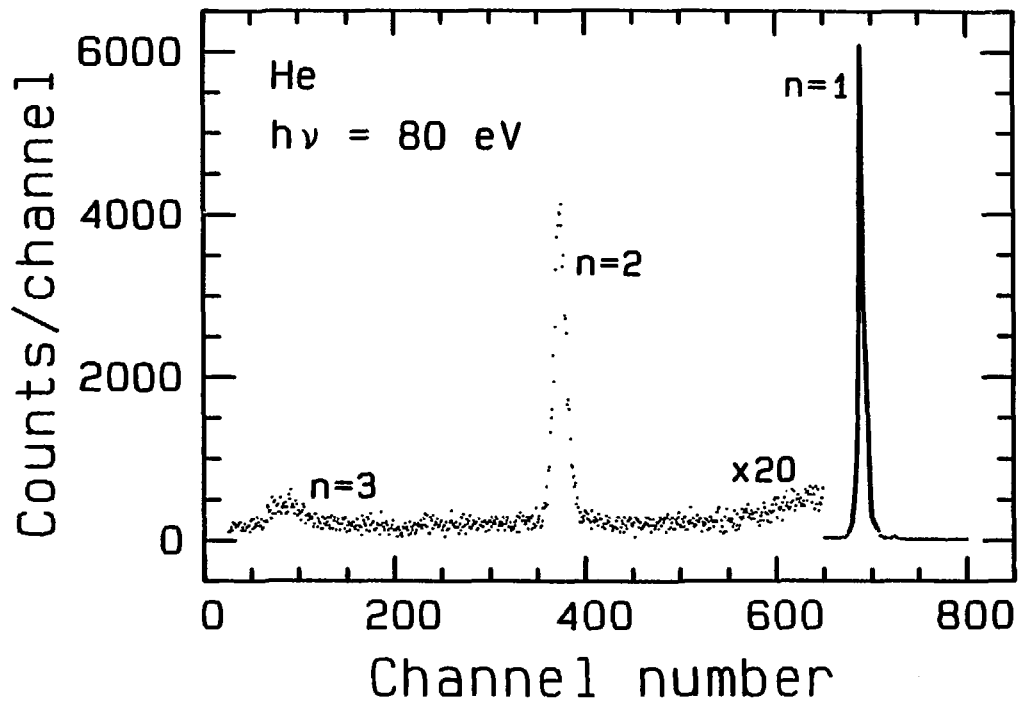
XBL 834-9462

Figure 3

Figure 4
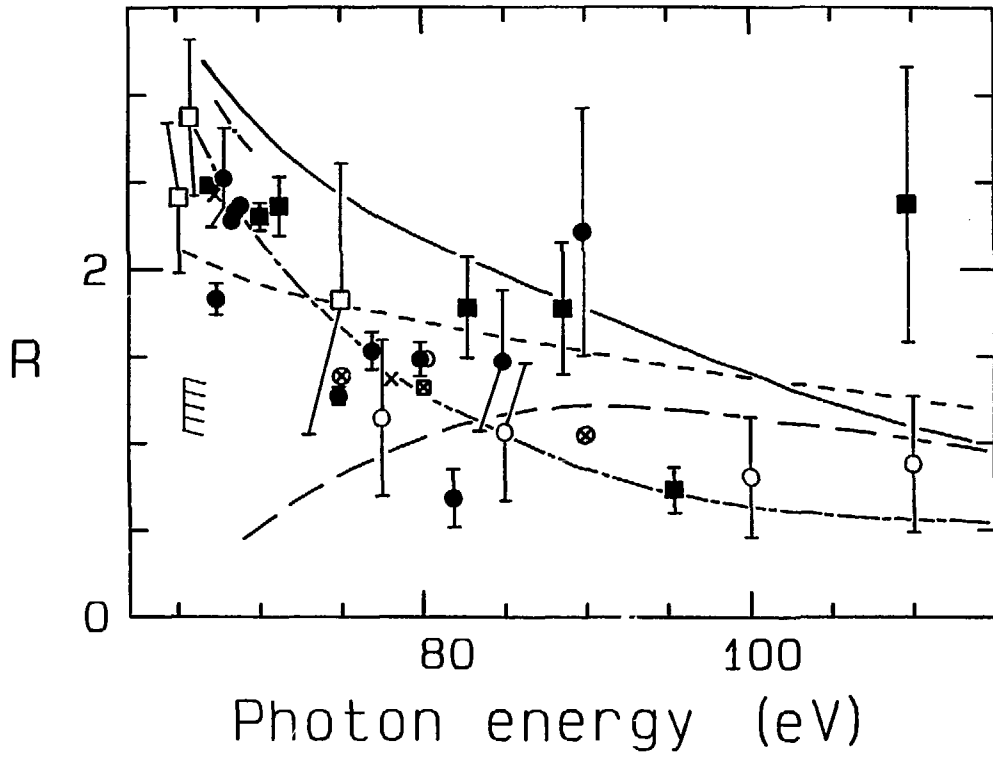
XBL 834-9463
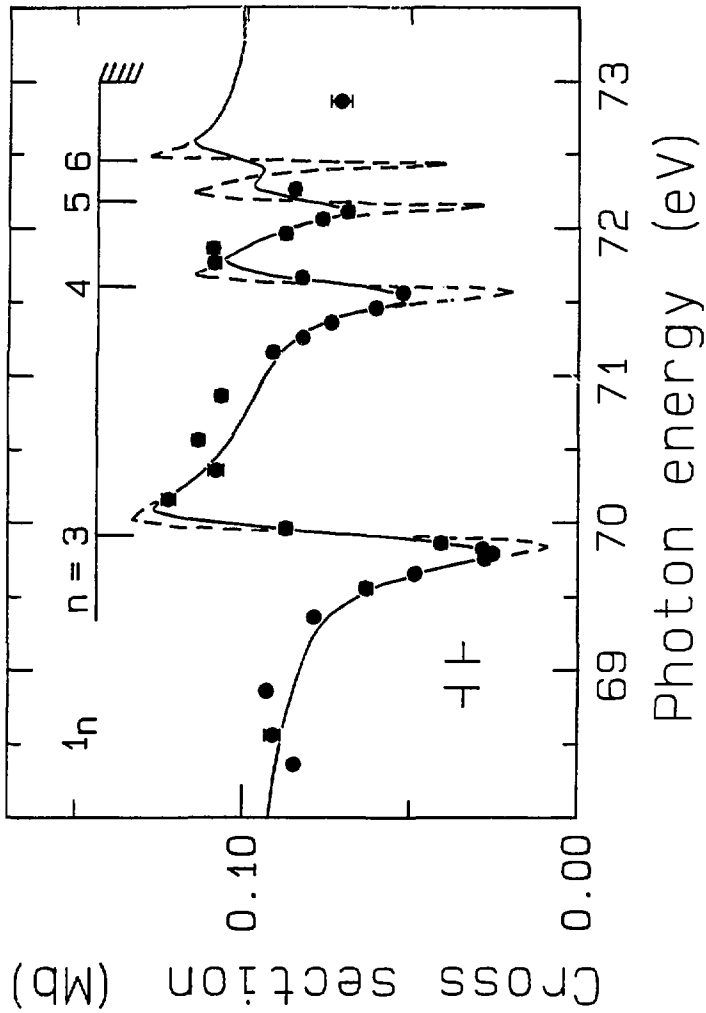
XBL 834-9464

Figure 5

Figure 6

XBL 834-9466
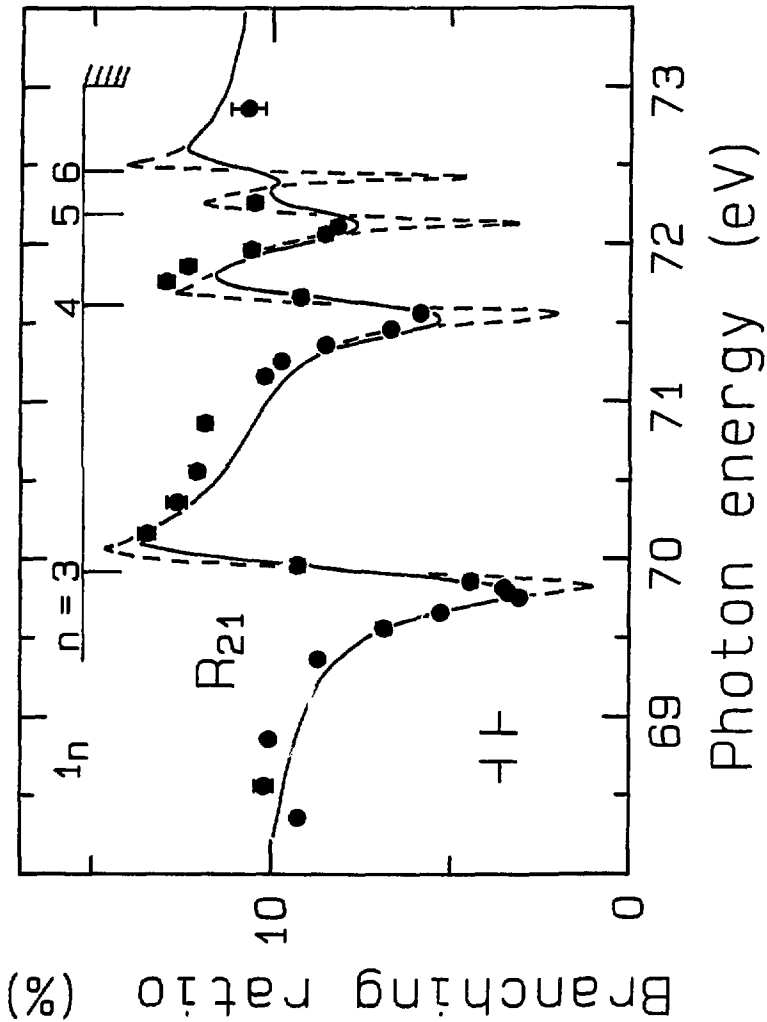
Figure 7
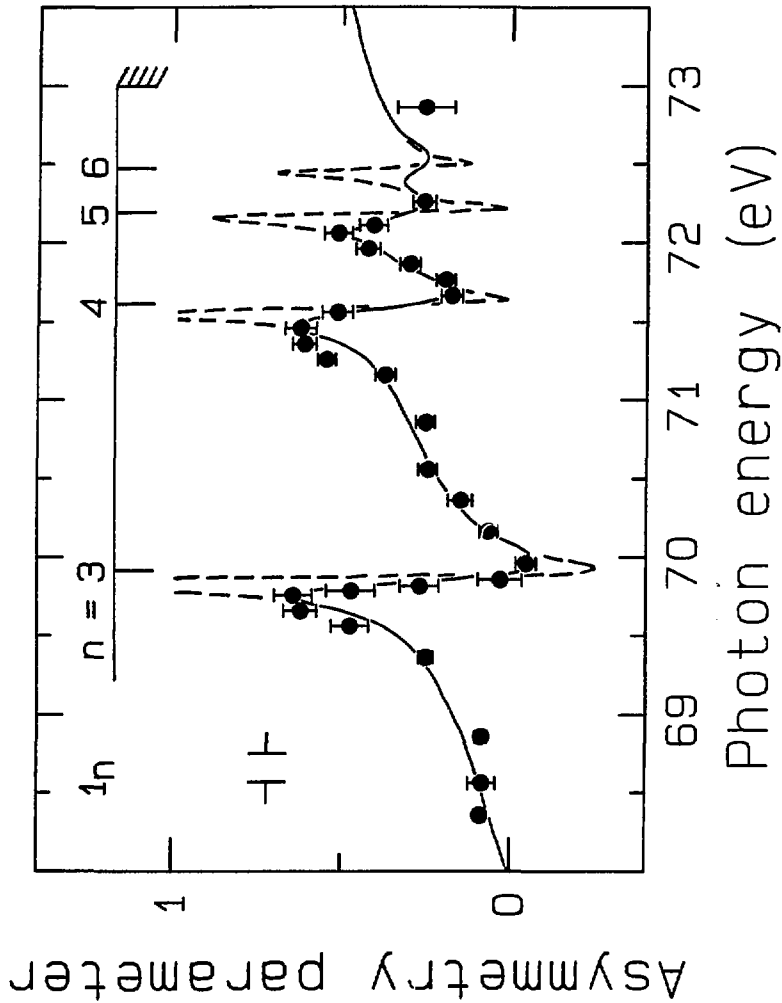
XBL 834-9467

Figure 8

XBL 834-9468

ACKNOWLEDGEMENTS

I wish to thank my research director, Dave Shirley, for providing a conducive atmosphere within which to pursue my interests. His scientific insight and willingness to allow me to follow my own path were especially appreciated.

All of the work in this dissertation was a collaborative effort with several people. The most significant contributions were provided by Steve Southworth, Paul Kobrin, and Carlton 'Trues' Truesdale; my colleagues for most of my time at Berkeley. Valuable assistance also has been given by Trish Ferrett, Phil Heimann, Uwe Becker, Bill Brewer, Hans Kerkhoff, and Shige Owaki. Special thanks to Paul Kobrin for making those long shifts at SSRL a little less unbearable.

I also benefited from the experience of Dennis Trevor and Jim Pollard, older students who always had the answers. The remainder of the Shirley group, especially Wini Heppler and Barbara Moriguchi, also has been helpful.

My parents and family have been very supportive throughout my graduate career. Their encouragement, caring and love has helped to keep me going. I especially want to thank Steve, Carolyn, Ron, Maxine, Loren, and Trish; my closest friends during the last 5 years.